ANALYSES OF THERMO-ACTIVE PILES CONSIDERING SURFACE RADIATION AND WIND CONVECTION EFFECTS

by

Semra Polat

B.S., Civil Engineering, Istanbul Technical University, 2021

Submitted to the Institute for Graduate Studies in
Science and Engineering in partial fulfillment of
the requirements for the degree of
Master of Science

Graduate Program in Civil Engineering
Boğaziçi University

2024

ACKNOWLEDGEMENTS

Firstly, I would like to express my sincere gratitude to my advisor, Prof. Özer Çinicioğlu, and my co-advisor Dr. Melis Sütman, for their continuous support, guidance, and encouragement throughout the duration of my master's research. Their insightful feedback and unwavering patience were instrumental in the successful completion of this thesis.

I would also like to thank Prof. Kutay Orakçal and Assoc. Prof. Aslı Yalçın Dayıoğlu for serving on my thesis committee and providing insightful feedback.

Special thanks go to my colleagues, Mert Güner, and Uğur Can Erginağ, for their collaborative spirit, and the countless discussions that enriched my research experience.

Above all, I am profoundly thankful to my family for their unwavering encouragement and belief in my abilities. Their constant presence and support have been an enduring source of strength and motivation.

Finally, I would like to acknowledge the financial support provided by TÜBİTAK (The Scientific and Technological Research Council of Türkiye) under the BİDEB 2210-A program.

ABSTRACT

ANALYSES OF THERMO-ACTIVE PILES CONSIDERING SURFACE RADIATION AND WIND CONVECTION EFFECTS

Energy piles are emerging as a promising technology for utilizing shallow geothermal energy, garnering considerable interest recently. This has led to an increase in studies, including field tests, model tests, and numerical analyses. While numerical analyses are advantageous due to their flexibility, their accuracy depends on thorough validation with field or model data. This task is complex because of the intricate interactions between mechanical, thermal, and hydrological processes. The validation process is further complicated by factors such as cyclic thermal loading, seasonal temperature changes, and intermittent operation. It's important to note that many verification studies use adiabatic thermal boundary conditions, which ignore atmospheric temperature fluctuations and wind effects that significantly impact the thermal behavior of energy piles, particularly near the surface. This study addresses this limitation by incorporating atmospheric and solar effects into the numerical analysis, using a thermal loading test on a continuous flight auger pile in Houston, Texas. By considering surface solar radiation, this study improves the understanding of the thermal responses of soil and piles, producing results that closely match field measurements. Incorporating atmospheric and solar effects advances the accuracy and relevance of numerical models in simulating energy pile behavior, which is crucial for optimizing their energy efficiency and performance.

ÖZET

YÜZEY RADYASYONU VE RÜZGAR KONVEKSİYONUNUN ETKİLERİYLE TERMO-AKTİF KAZIKLARIN ANALİZİ

Enerji kazıkları, sığ jeotermal enerjiden yararlanmak için umut verici bir teknoloji olarak ortaya çıkmıştır ve son yıllarda büyük ilgi görmektedir. Bu ilgi, saha testleri, model testleri ve sayısal analizler dahil olmak üzere çalışmaların artmasına neden olmuştur. Sayısal analizler esneklikleri nedeniyle değerli olsa da, güvenilirlikleri saha veya model ölçekli verilerle titizlikle doğrulanmalarına bağlıdır. Bu doğrulama süreci, mekanik, termal ve hidrolojik süreçlerin karmaşık etkileşimleri nedeniyle zorludur. Döngüsel termal yükleme, mevsimsel sıcaklık değişimleri ve aralıklı çalışma gibi faktörler bu süreci daha da karmaşık hale getirmektedir. Bununla birlikte, birçok doğrulama çalışması adyabatik termal sınır koşullarını kullanarak atmosferik sıcaklık dalgalanmalarını ve rüzgar etkilerini göz ardı etmektedir ve bu durum, özellikle yüzeye yakın enerji kazıklarının termal davranışını önemli ölçüde etkilemektedir. Bu çalışma, bu eksikliği gidermek amacıyla atmosferik ve güneş etkilerini sayısal analize dahil etmekte ve Houston, Teksas'ta bir sürekli uç burgusu kazık üzerinde termal yükleme testini modellemektedir. Yüzey güneş radyasyonunu dikkate alan bu çalışma enerji kazıklarının termal tepkilerinin daha iyi anlaşılmasını sağlamıştır ve saha ölçümleriyle yüksek uyum gösteren sonuçlar üretmiştir. Atmosferik ve güneş etkilerini göz önünde bulundurarak, bu araştırma enerji kazıklarının davranışını simüle eden sayısal modellerin doğruluğunu ve uygulanabilirliğini artırmakta, bu da enerji verimliliği ve performanslarının optimize edilmesi açısından önem taşımaktadır.

TABLE OF CONTENTS

ACKNOWLEDGEMENTS iii
ABSTRACT iv
ÖZET v
LIST OF FIGURES viii
LIST OF TABLES xii
LIST OF SYMBOLS xiii
LIST OF ACRONYMS / ABBREVIATONS xv
1. INTRODUCTION 1
2. LITERATURE REVIEW 2
2.1. Geothermal Energy 2
2.2. Geothermal Systems 4
2.3. Energy Geostructures 4
2.3.1 Functioning of Energy Geostructures 5
2.4. Energy Piles 9
2.4.1. Thermo-Mechanical Behavior of Energy Piles 11
2.4.2. Modelling Approaches for Energy Piles 18
2.5. Ground Heat Flow Mechanisms 19
2.5.1. Conduction 19
2.5.2. Convection 20
2.5.3. Radiation 21
3. FIELD TEST 23
3.1. Site Description 23
3.2. Instrumentation 25
3.3. Schedule of In-Situ Tests 27
3.4. Test Results 27
4. NUMERICAL MODEL 30
4.1. Description of The Model 30
4.2. Model Geometry 30
4.3. Modelling Assumptions 32

4.4. Governing Equations 33
4.5. Boundary and Initial Conditions 35
4.6. Mesh 36
4.6.1. Skewness 37
4.6.2. Maximum Angle 37
4.6.3. Growth Rate 38
4.7. Model Development 38
4.7.1. The Positioning of The Sensors 38
4.7.2. Incorporation of Solar Radiation and Wind Convection 39
4.7.3. Pre-Analysis Evaluation: With and Without Solar Radiation and Wind. 40
5. FIELD RESULTS AND NUMERICAL VALIDATION 44
6. DISCUSSIONS 55
6.1. Different Contributions of Solar Radiation and Wind 55
6.2. Applicability of This Modelling Approach 57
7. CONCLUSIONS 58
REFERENCES 61
APPENDIX A: PERMISSION INFORMATION 73

LIST OF FIGURES

Figure 2.1. Variation of ground temperatures with depth in Istanbul, Maslak in 2012 (modified after Aydin et al, 2013)..... 3

Figure 2.2. Illustration of the typical temperature gradient with increasing depth in the Earth's subsurface (modified after Banks, 2012). 3

Figure 2.3. Shallow energy geostructures (energy piles, energy tunnels and energy shoring). 6

Figure 2.4. Heat pump system and associated operation for the heating of a building. 7

Figure 2.5. Illustration of U, W and spiral shaped pipe configurations embedded in energy piles. 8

Figure 2.6. General applications of pipe configurations for energy tunnels. 9

Figure 2.7. General applications of pipe configurations for energy tunnels. 9

Figure 2.8. Thermo-mechanical behavior of a free body pile subjected to heating and cooling (modified after Bourne-Webb et al., 2012). 12

Figure 2.9. Thermo-mechanical behavior of a pile subjected to heating and cooling with shaft friction present (modified after Bourne-Webb et al., 2012)..... 13

Figure 2.10. Thermo-mechanical behavior of a pile subjected to heating and cooling with end-restraint (modified after Bourne-Webb et al., 2012)..... 15

Figure 2.11. Thermo-mechanical behavior of a friction pile subjected to heating and cooling with mechanical load on top (modified after Soga and Rui, 2016). 16

Figure 2.12. Thermo-mechanical behavior of an end-bearing pile subjected to heating and cooling with mechanical load on top (modified after Soga and Rui, 2016). 17

Figure 3.1. Layout of experimental site in Houston, Texas (Sutman, 2016). 24

Figure 3.2. Pile and soil profile (modified after Sutman et al., 2019). 25

Figure 3.3. Arrangement of the sensors and pipes within the pile (Sutman, 2016). 26

Figure 3.4. Cross-sectional layout of the sensors within the pile (modified after Sutman et al., 2019). 26

Figure 3.5. Thermal loads applied to the pile (modified after Sutman et al., 2019). 27

Figure 3.6. Temperature profiles along the pile during the first episode of heating and cooling (modified after Sutman et al., 2019). 28

Figure 3.7. Thermally induced axial stresses along the pile during the first episode of heating and cooling (modified after Sutman et al., 2019). 29

Figure 4.1. 3D view of the model. 31

Figure 4.2. 3D view of the pile and line elements that represent pipes. 32

Figure 4.3. Mechanical boundary conditions applied to the model. 35

Figure 4.4. Comparison of measured and calculated outlet temperatures. 36

Figure 4.5. General view of the mesh applied to the model. 37

Figure 4.6. Ambient temperatures and wind speed for the two months preceding and during the field test at William P. Hobby weather station (ASHRAE, 2013). 39

Figure 4.7. Initial field temperatures prior to the test obtained by simulations (a) with solar radiation and wind effects, (b) without the solar radiation and wind effects. 41

Figure 4.8. Temperature measurements on the 1st day of heating from simulations with and without solar radiation and wind effects: (a) at D=11.7 cm, (b) at D= 12.9 cm. 42

Figure 4.9. Thermally induced axial stress measurements on the 1st day of heating from simulations with and without solar radiation and wind effects: (a) at D=11.7 cm, (b) at D= 12.9 cm. 43

Figure 5.1. Comparison of temperatures and stresses along the pile between the field test and numerical analysis for day-1. 47

Figure 5.2. Comparison of temperatures and stresses along the pile between the field test and numerical analysis for day-2. 48

Figure 5.3. Comparison of temperatures and stresses along the pile between the field test and numerical analysis for day-3. 49

Figure 5.4. Comparison of temperatures and stresses along the pile between the field test and numerical analysis for day-4. 50

Figure 5.5. Comparison of temperatures and stresses along the pile between the field test and numerical analysis for day-5. 51

Figure 5.6. Comparison of temperatures and stresses along the pile between the field test and numerical analysis for day-6. 52

Figure 5.7. Comparison of temperatures and stresses along the pile between the field test and numerical analysis for day-7. 53

Figure 5.8. Thermally induced axial stresses in pile cross-section on day-3 at (a) 5.7m depth, (b) 8.7m depth, (c)11.6 m depth, (d) 14.5m depth. 54

Figure 6.1. Comparison of temperature profiles along the pile obtained in the field and with analyses with solar radiation only, wind convection only and combined effects. 56

Figure A.1. Permission mail received from Melis Sutman. 73

LIST OF TABLES

Table 3.1. Thermal and mechanical properties of soil layers, pile and pipes. 24

Table 4.1. Summary of mesh element quality..... 38

LIST OF SYMBOLS

A	Area
A_p	Pipe cross sectional area
C	Volumetric heat capacity
C_l	Volumetric heat capacity of heat exchanger fluid
C_2	Auxiliary radiation constant
D	Distance from the pile center
D_{ijkl}	Elastic stiffness tensor
E	Young's modulus
F_v	Volume force factor
f_d	Coefficient of friction
G	Irradiation
h	Convective heat transfer coefficient
h_{eff}	Coefficient of pipe wetted perimeter for the heat transfer
h_{int}	Convective heat transfer coefficient of inner surface of pipe
Nu	Nusselt number
$Nu_{turbulent}$	Nusselt number for turbulent flow in pipes
Q	Conductive heat flux
q_{conv}	Convective heat flux
q_r	Net inward radiative heat flux
q_w	Convective heat flux by wind
Q_{wall}	Heat flux per unit pipe length
r	Refractive index
r_{ext}	External pipe radius
r_{int}	Internal pipe radius
s	Specular reflected radiation
T	Temperature
T_l	Temperature of the heat exchanger fluid
T_{ext}	Temperature of the outer surface of the pipe

T_f	Temperature of the fluid
T_{ref}	Reference temperature
T_s	Temperature of the surface
u_l	Velocity of the heat exchanger fluid
χ_r	Total radiosity
α	Coefficient of thermal expansion
α_r	Diffuse reflectivity
β_{kl}	Vector of linear thermal expansion coefficient
γ	Unit weight
$\varepsilon_{blocked}$	Blocked strain
ε_{free}	Free thermal strain
ε_{kl}	Total strain tensor
ε_{obs}	Observed strain
ε_r	Emissivity
θ	Angle over an edge
θ_e	Angle of the corresponding edge
λ	Thermal conductivity coefficient
λ_i	Upper limit of a wavelength at a given frequency
λ_{i-1}	Lower limit of a wavelength at a given frequency
λ_l	Thermal conductivity of the heat exchanger fluid
λ_p	Thermal conductivity of the pipe
μ	Liquid dynamic viscosity
ν	Poisson ratio
ρ	Density
ρ_l	Density of heat exchanger fluid
σ_{ij}	Total stress tensor
σ_r	Boltzmann constant
σ_{th}	Thermally induced axial stress

LIST OF ACRONYMS / ABBREVIATONS

3D	Three-dimensional
ASHRAE	American Society of Heating Refrigerating and Air-Conditioning Engineers
CFA	Continuous Flight Auger
COP	Coefficient of Performance
PEX	Crosslinked polyethylene
TP-1	Test Pile 1
TP-2	Test Pile 2
TP-3	Test Pile 3
VWSG	Vibrating Wire Strain Gage

1. INTRODUCTION

The exploration of geothermal energy as a sustainable resource has gained significant attention in recent years due to its continuous availability and minimal environmental impact. Unlike intermittent sources such as wind and solar energy, geothermal energy provides a steady and reliable supply, making it a crucial component in the development of energy-efficient infrastructures, particularly in smart cities. Geothermal energy is derived from the natural heat stored within the Earth's crust, which originates from the planet's formation, radioactive decay, and solar energy absorption. This heat can be harnessed through various geothermal systems, classified as shallow or deep based on their operational depths.

The utilization of geothermal systems, especially in the form of energy geostructures, represents an innovative approach to integrating energy transfer capabilities with structural support functions. These systems, which include energy piles, diaphragm walls, and tunnel linings, leverage the relatively stable ground temperatures found below the Earth's surface to provide heating and cooling for buildings, contributing to climate control and reducing reliance on fossil fuels (Di Donna et al., 2020).

This study aims to enhance the numerical modeling of energy piles by incorporating atmospheric and solar effects, thereby improving the accuracy of thermal response predictions. By modeling a thermal loading test conducted on a single pile in Houston, Texas (Sutman, 2016), this research seeks to replicate real-world conditions and validate the model against field data. The inclusion of surface solar radiation and wind convection in the numerical analysis allows for a more precise representation of the thermal behavior of both soil and pile, ultimately leading to a better understanding of temperature changes and thermally induced stresses within the energy pile. This improved modeling approach can significantly contribute to the design and implementation of more efficient and reliable geothermal energy systems in various built environments.

2. LITERATURE REVIEW

2.1. Geothermal Energy

Geothermal energy refers to the heat naturally stored in the Earth's crust. This natural heat originates from three primary sources: the planet's formation, the decay of radioactive minerals, and the absorption of solar energy at the surface (Banks, 2012). The ground temperature typically influenced by atmospheric conditions up to a depth of 10 meters. Below that region, the temperature remains nearly constant throughout the year and can be considered equivalent to the annual average outside air temperature (Kalagirou and Florides, 2005). Therefore, beyond a certain depth, the ground tends to be warmer than the atmosphere in winter and cooler in summer.

Figure 2.1 provides an example of ground temperature profile for the climate region of Istanbul, where surface temperature varies around 20°C throughout the year. At a depth of 8 meters, seasonal temperature fluctuations remain within 1°C range. As depth increases into the Earth’s interior, temperature rises gradually due to the geothermal gradient, typically ranging from approximately 1 to 3 °C per 100 meters (see Figure 2.2), with exceptions found in anomalous or volcanically active regions (Banks, 2012). focus of extensive research by civil engineers and various approaches to assess the stability of the slopes have been developed.

Unlike wind and solar energy, which can vary with weather conditions, geothermal energy offers continuous and reliable availability everywhere on Earth. Its processes result in minimal or no greenhouse gas emissions due to the absence of chemical reactions like combustion during conversion and utilization (Lee et al., 2007). Consequently, geothermal energy presents a viable alternative to fossil fuels, reducing the environmental footprint of energy production and contributing to climate change mitigation efforts. Additionally, its characteristic of providing a steady and reliable energy supply positions geothermal energy as a key component in the development of smart cities, particularly in the domain of building climate control (Acharjya et al., 2024).

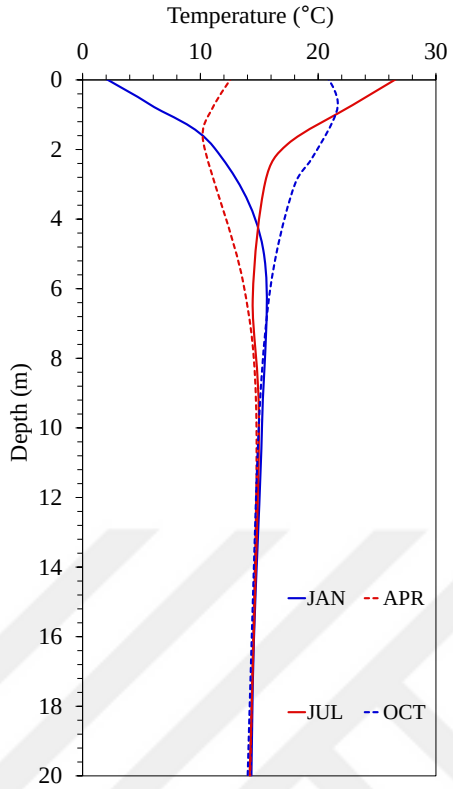


Figure 2.1. Variation of ground temperatures with depth in Istanbul, Maslak in 2012 (modified after Aydin et al, 2013).

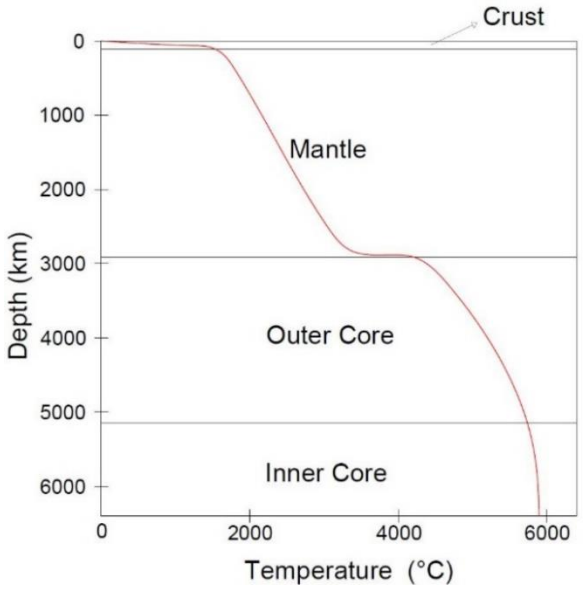


Figure 2.2. Illustration of the typical temperature gradient with increasing depth in the Earth's subsurface (modified after Banks, 2012).

2.2. Geothermal Systems

Geothermal systems are advanced technological systems engineered to harness geothermal energy. These systems are composed of three primary elements: a heat source, a heat sink, and a heat exchanger. Normally, the ground serves as the heat source and a structural element acts as the heat sink. However, there are instances where these roles can be reversed. The heat exchanger is a component that enables the transfer of heat between the heat source and the heat sink using a fluid.

Geothermal systems are classified into two main categories: shallow geothermal systems and deep geothermal systems. The utilizations of geothermal systems are broadly classified into power generation, use for heating and air conditioning and heat storage. The distinction between shallow and deep geothermal systems is based on the operational depth, with shallow systems operating at depths of less than 400 meters and deep systems at depths exceeding 400 meters.

Shallow geothermal systems typically operate with low temperature and enthalpy, rendering them suitable for applications such as residential and commercial heating, cooling. These systems include energy geostructures, vertical geothermal boreholes, groundwater capture systems, geothermal baskets, and horizontal geothermal boreholes. Conversely, deep geothermal systems such as thermal springs, hydrothermal systems, and petrothermal systems operate with medium to high temperature and enthalpy, which are predominantly utilized for power generation (Laloui and Rotta Loria, 2020).

2.3. Energy Geostructures

Energy geostructures represent a cutting-edge, multifunctional technology designed to facilitate energy transfer and provide structural support across various structure types. These systems, encompassing sub-surface structures like pile foundations, barrettes, diaphragm walls, base slabs, tunnel linings, and anchors, are adept at conducting heat transfer with the ground (Batini et al., 2015; Sanchez et al., 2017; Akrouch et al., 2020; Najma and Sharma, 2021; Makasis and Narsilio, 2021; Li et al., 2021; Kong et al., 2021; Lou et al., 2021;

Adinolfi et al., 2021). They utilize the relatively low-grade thermal energy available just beneath the Earth's surface, often integrated with heat pumps to effectively harness this geothermal energy. As a type of shallow geothermal system, energy geostructures merge the dual capabilities of structural reinforcement and thermal energy exchange within a closed system, making them suitable for a range of built environments.

Integrating geostructures and geothermal heat exchangers in a single construction phase can offer cost savings over building them separately. Additionally, energy geostructures differ from traditional geothermal systems in terms of construction materials. They are made of concrete, which possesses superior thermal properties compared to the materials like bentonite used in conventional geothermal technologies (Di Bari, 2019). This advantage enhances the efficiency of heat exchange in energy geostructures relative to their conventional counterparts. Therefore, this innovative strategy not only leverages the thermal properties of the ground but also contributes to ecological sustainability by offering solutions that address environmental challenges. The development and implementation of energy geostructures have been significantly influenced by the growing demand for environmentally friendly energy alternatives (Bayer et al., 2019; Sani et al., 2019).

2.3.1 Functioning of Energy Geostructures

Energy geostructures are composed of traditional geotechnical structures such as piles, tunnels, with one or multiple embedded piping circuits designed to facilitate thermal exchange with the ground. Geostructures that are frequently used for this purpose are piles, tunnels, and shoring structures/basement walls. These structural elements are illustrated in Figure 2.3.

Energy geostructures operate by taking advantage of the temperature differences depending on the depth in the soil. In the upper layers of the ground, specifically within the first 6 meters, the temperature is highly responsive to changes in atmospheric conditions, exhibiting variations due to diurnal (day-night) and seasonal cycles. Below these initial meters, ground temperature stabilizes and is generally unaffected by surface atmospheric changes, and the temperature remains constant year-round, ranging from 10°C to 25°C,

which varies depending on the geographical latitude of the region. Hence, in winter, the ground is warmer relative to the colder air above, and in summer, it is cooler than the air, making these temperature differentials crucial for the functioning of energy geostructures (Narsilio et al., 2014). Energy geostructures facilitate heat exchange with the ground for various applications, including regulating temperature for comfort in living spaces, providing hot water for domestic or agricultural use, and maintaining anti-frost heating systems in transportation infrastructures like roads, bridges, and airports (Brandl, 2006).

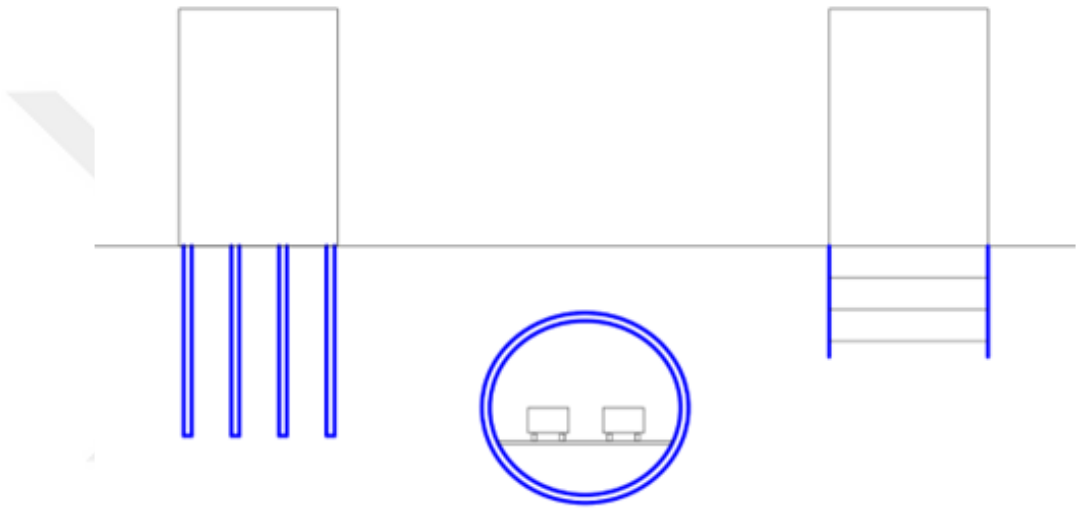


Figure 2.3. Shallow energy geostructures (energy piles, energy tunnels and energy shoring).

Figure 2.4 illustrates the operational mechanism of an energy geostructure for a building, where heat is extracted from the ground using a circulating heat carrier fluid — typically water or a water-antifreeze mixture—within pipes embedded in a geostructure. Ground source heat pumps are used for heat exchange between ground and superstructure. The system includes ground source heat pumps for facilitating heat exchange between the ground and the superstructure, operating across two circuits. The primary circuit, or the ground heat exchange system, manages the heat transfer between the ground and the geostructure, while the secondary circuit is responsible for air conditioning within the superstructure and for hot water production. The heat pump, depicted in Figure 2.4, operates based on the principle that compressing a fluid increases its temperature, converting mechanical energy into heat through electrical input. Utilizing a refrigerant fluid, the system

undergoes four stages: Initially, in the evaporator, the refrigerant absorbs heat from the ground's heat carrier fluid, transitioning into a gas while the cooled heat carrier fluid returns to the ground for reheating. Subsequently, the compressor elevates the gas's temperature and pressure through electrical compression. In the condenser stage, heat transfers from the refrigerant to a secondary circuit's heat carrier fluid. Finally, the refrigerant passes through an expansion valve to restore its initial temperature and pressure, initiating the next cycle.

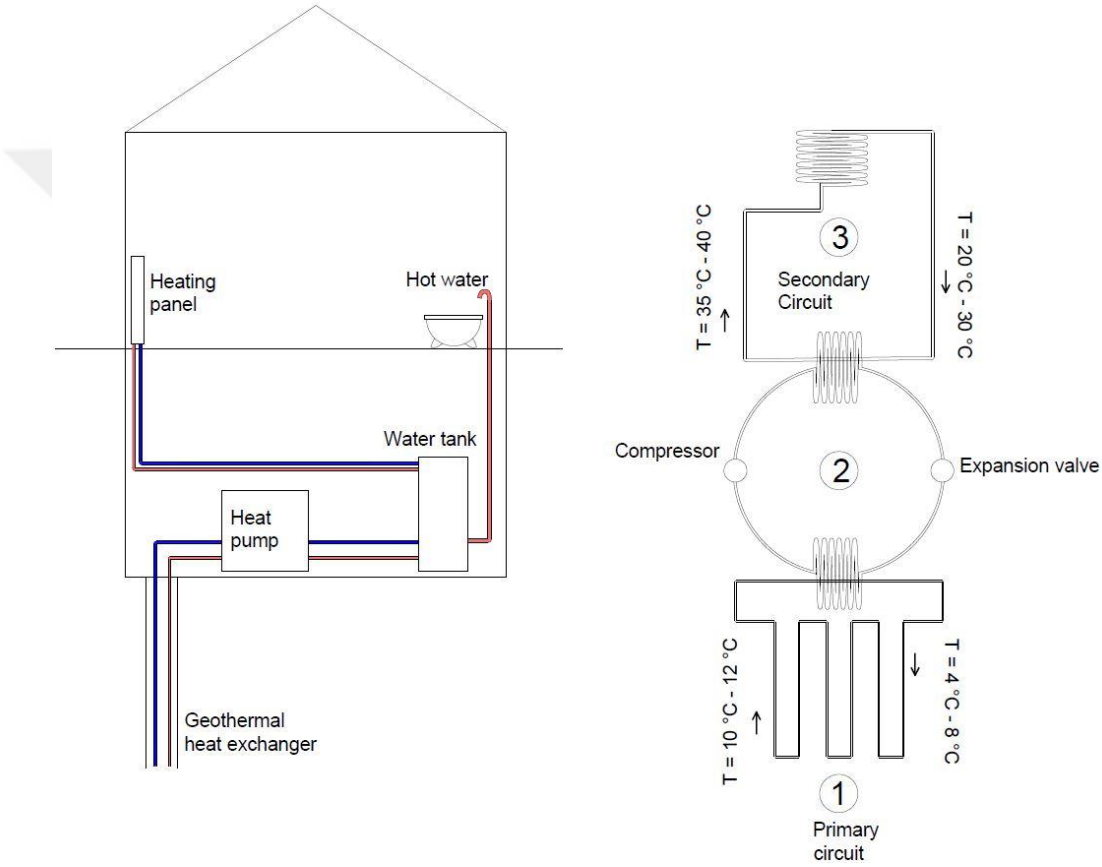


Figure 2.4. Heat pump system and associated operation for the heating of a building.

The efficiency of these structures can be quantified by using a coefficient of performance, COP, which defines how many units of heat can be generated for every unit of electricity used. Typically, energy geostructures have a COP in the 3.5-4 range (Brandl, 2006). It is calculated as

$$COP = \frac{Energy\ output\ after\ heat\ operation\ [kW]}{Energy\ input\ for\ heat\ pump\ operation\ [kW]}. \quad (2.1)$$

In energy geostructures, various pipe configurations can be designed considering energy needs, installation conditions, and operation and cost factors. Among the pipe configurations used for energy piles, single U-shaped, double U-shaped, multi-U-shaped, W-shaped, and spiral configurations can be mentioned, and illustrations of the pipe configurations are presented in Figure 2.5. Among them, the spiral pipe configuration, although it has a higher heat transfer potential, is less frequently chosen due to installation difficulties, while the multi-U-shaped configuration is often preferred (Mohamad et al., 2021).

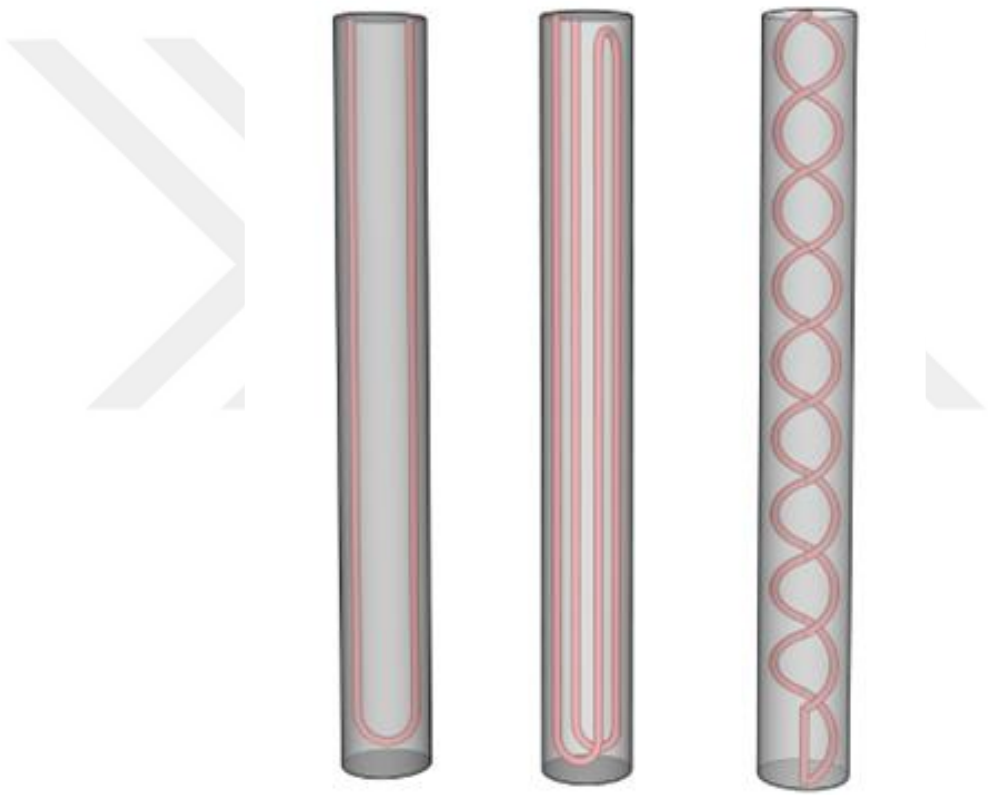


Figure 2.5. Illustration of U, W and spiral shaped pipe configurations embedded in energy piles.

In energy tunnels, pipes can be designed parallel or perpendicular to the tunnel's axial direction (see Figure 2.6) (He et al., 2023). In energy walls and energy slabs, the arrangement of the heat exchange surface is often preferred to be either lateral or vertical (see Figure 2.7) (Makasis and Narsilio, 2020).



Figure 2.6. General applications of pipe configurations for energy tunnels.

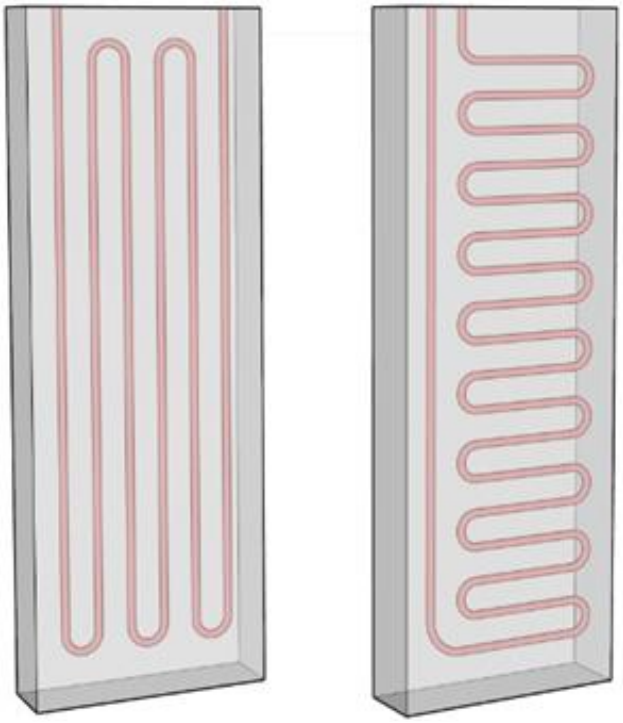


Figure 2.7. General applications of pipe configurations for energy tunnels.

2.4. Energy Piles

Energy piles are the most used type of energy geostructure. These systems function as the primary circuit, with heat exchangers embedded within the piles themselves. Additionally, a secondary pipe network circulates heat energy to and from the building,

complemented by a heat pump that adjusts temperatures to suit the building's requirements. Constructively, energy piles incorporate high-density polyethylene pipes. In bored piles, these pipes are typically attached to the reinforcement cage, while in continuous flight auger piles, they are inserted into the center of the piles (Soga and Rui, 2016).

In recent years, there has been a notable rise in the number of studies focusing on energy piles. These studies include full-scale field tests that examine single pile behavior and thermally induced axial-radial stresses under both monotonic and cyclic thermal loading (Bourne-Webb et al., 2009; Wang et al., 2015, 2017; Faizal et al., 2018; Sutman et al., 2019; Moradshahi et al., 2022; Zhou et al., 2023), as well as pile efficiency (Zarrella et al., 2017; Luo et al., 2019) and pile groups with structural cover (Mimouni and Laloui, 2015; Rotta Loria and Laloui, 2018; Faizal et al., 2019; Wu et al., 2020; Fang et al., 2020, 2022; Li et al., 2022; Moradshahi et al., 2022). Additionally, centrifuge tests have been conducted to evaluate the impact of thermal loading on the shaft and end bearing resistance of energy piles (Stewart and McCartney, 2014; Ng et al., 2015, 2021; Vitali et al., 2022). Furthermore, 1g model scale tests have investigated how both cyclic and monotonic thermal loads, whether heating or cooling, affect the load-displacement response of piles and induce corresponding thermally induced axial and radial strains along the pile (Wang et al., 2017; Huang et al., 2018; Yazdani et al., 2019; Elzeiny and Suleiman, 2021; Kong et al., 2021; Zhao et al., 2022; Peng et al., 2023). These studies indicate that heating reduces the shaft capacity of piles in granular soils, but the end bearing capacity tends to increase with rising accumulated vertical deformations.

In terms of numerical analyses, various techniques such as finite difference, finite element, and finite volume approaches have been employed. These tools have facilitated studies on pile efficiency with corresponding heat transfer estimation (Cui and Zhu, 2017; Zhang and Chen, 2017; Dehghan, 2018; Park et al., 2018), development of thermal pile load-transfer curves (Rotta Loria and Laloui, 2017; Sutman et al., 2019; Liu et al., 2023), thermally induced axial and radial stresses along energy piles (Li et al., 2017; Moradshahi et al., 2021; Shao et al., 2021; Saggu and Sarma, 2023), and the behavior of both single and groups of piles under cyclic thermal loading (Arzanfudi et al., 2020; Behbehani and McCartney, 2022; Faizal et al., 2022; Heidari et al., 2022; Zhao et al., 2022). Numerical

analyses provide several advantages, including flexible adjustment of boundary conditions and consideration of various scenarios in a more efficient and cost-effective manner. However, like all numerical studies, their ability to produce reliable results must be validated. This typically involves modelling a field or model test and comparing the responses. This task is complex as it requires defining all mechanical, thermal, and hydrological effects (Laloui et al., 2006; Knellwolf et al., 2011; Perić et al., 2017; Rotta Loria and Laloui, 2017; Moradshahi et al., 2021; Faizal et al., 2022). Additionally, the thermal loading scenarios considered can be monotonic or cyclic. Seasonal temperature fluctuations and intermittent operations contribute to cyclic thermal loading, further complicating the problem (Brandl, 2006; Yi et al., 2008; Wood et al., 2010; Dai et al., 2015; McCartney and Murphy, 2017; Sutman et al., 2019; Faizal et al., 2022; Peng et al., 2023).

2.4.1. Thermo-Mechanical Behavior of Energy Piles

Temperature changes associated with the operation of energy piles introduce further complications from structural and geotechnical standpoints. Thermal expansion is the phenomenon where materials alter their shape, size, and volume in response to temperature fluctuations. As materials heat up, their particles accelerate and spread further apart, resulting in expansion due to heightened kinetic energy. Conversely, when materials cool down, their particles decelerate and draw closer together, causing the material to shrink. This behavior can be observed in energy piles when they are free from any constraints. Consequently, if the pile is heated or cooled in the absence of surrounding soil, it will expand both vertically and radially, resulting in free thermal strains (Soga and Rui, 2016). The magnitude of this phenomenon depends on the temperature change and the material's thermal expansion coefficient as can be calculated as

$$\varepsilon_{free} = \alpha\left(T - T_{ref}\right) \tag{2.2}$$

where ε_{free}, α, T and T_{ref} are free thermal strain, coefficient of thermal expansion, applied temperature and reference temperature at in-situ conditions, respectively. Free thermal strain results in expansion due to heating and contraction due to cooling, as illustrated in Figure 2.8. These thermal strains alter the pile's geometry without mobilizing any axial load.

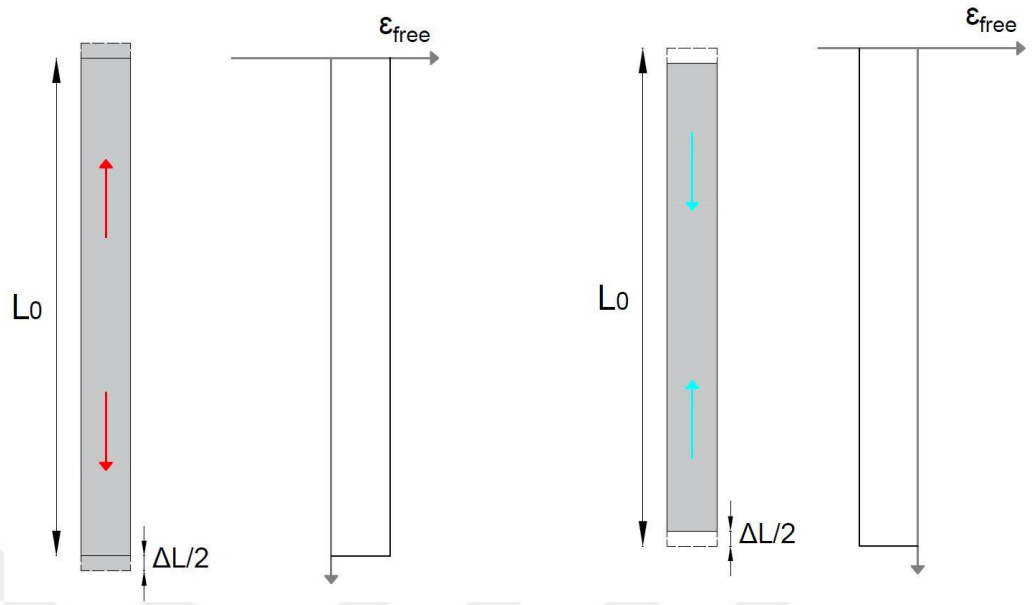


Figure 2.8. Thermo-mechanical behavior of a free body pile subjected to heating and cooling (modified after Bourne-Webb et al., 2012).

In reality, energy piles are not free from constraints; they are surrounded by soil and subject to mechanical loads. Consequently, temperature changes can induce blocked strains due to the restricted expansion or contraction at the boundaries. The blocked strain is defined as

$$\varepsilon_{blocked} = \varepsilon_{free} - \varepsilon_{obs} \tag{2.3}$$

where ε_{obs} is the observed strain of the pile. The blocked strains induce local stresses in the pile. It is called thermally induced stress and defined as

$$\sigma_{th} = E \cdot \varepsilon_{blocked} \tag{2.4}$$

where σ_{th} is thermally induced axial stress and E is Young's modulus of the pile.

The impact of surrounding soil and end-restraint without a mechanical load on the pile's response during heating and cooling are described in Figure 2.9 and Figure 2.10, respectively. As the strength and stiffness of the soil increase, the restraint at the pile-soil interface also increases. During heating, expansive strains at the pile's mid-depth are more suppressed than at the ends. In a stiffer soil profile, this results in larger compressive axial loads and greater mobilized shaft resistance. Conversely, during cooling, soil restraint suppresses contractive strain, leading to the development of tensile loads as soil resistance increases, assuming other conditions remain unchanged.

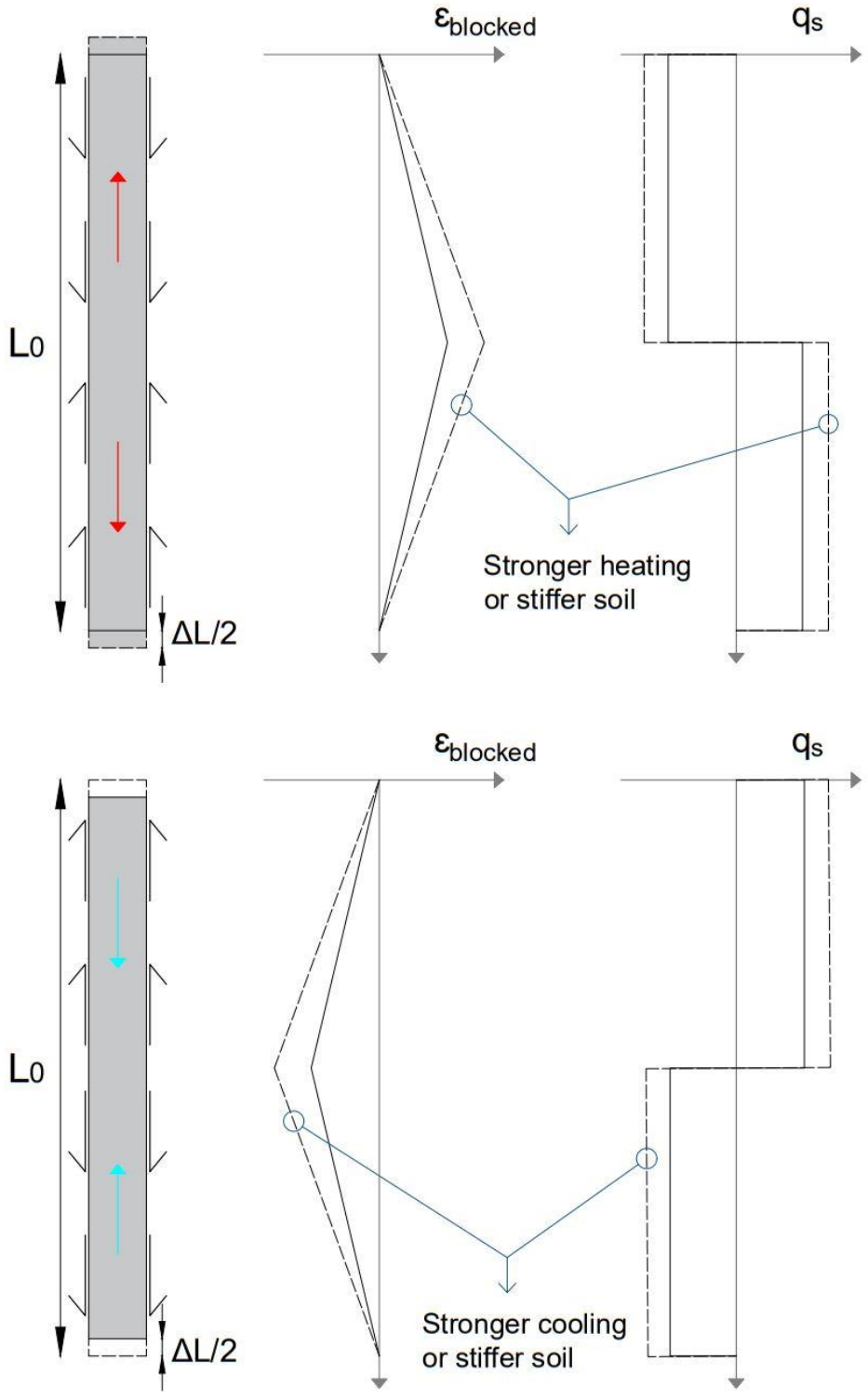


Figure 2.9. Thermo-mechanical behavior of a pile subjected to heating and cooling with shaft friction present (modified after Bourne-Webb et al., 2012).

End-restraint is provided by the superstructure and any loading at the pile head and can also occur due to a very stiff bearing layer at the pile toe, such as a rock socket. During heating, any restraint at the pile ends restricts expansive strains, generating compressive strains. The resulting strain and load profile depend on the stiffness of the end-restraints. Because axial deformation is limited, mobilized shaft resistance in a given soil is less than it would be without end-restraint. As end-restraint increases, mobilized shaft resistance decreases, approaching a scenario where the body is perfectly restrained; in this case, axial loads are maximized, and mobilized shaft resistance is zero. During cooling, the responses reverse.

A more realistic scenario is when the piles are subjected to mechanical load. Figure 2.11 illustrates the response of friction piles to heating and cooling under mechanical load. When heated, the upper half of the pile moves upward and the lower half downward, increasing friction. Cooling reverses these movements, potentially causing tension in parts of the pile, which is an important factor in design. Figure 2.12 presents the anticipated behavior of end-bearing piles under heating and cooling. Heating causes upward displacement similar to friction piles, with compressive thermal stress increasing with depth, thereby reducing shaft friction and increasing load transfer to the bottom. Cooling has the opposite effect without causing tension.

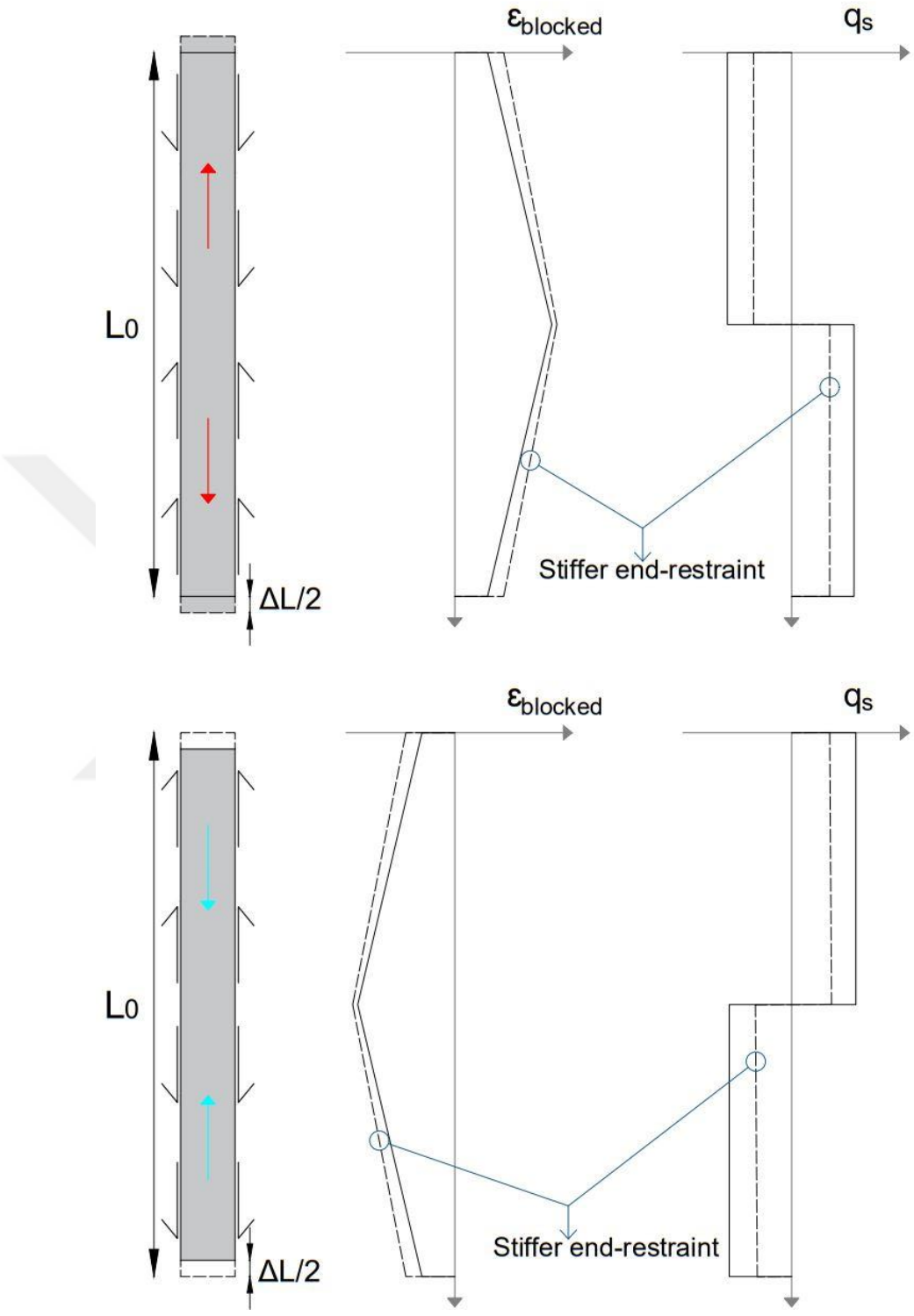


Figure 2.10. Thermo-mechanical behavior of a pile subjected to heating and cooling with end-restraint (modified after Bourne-Webb et al., 2012).

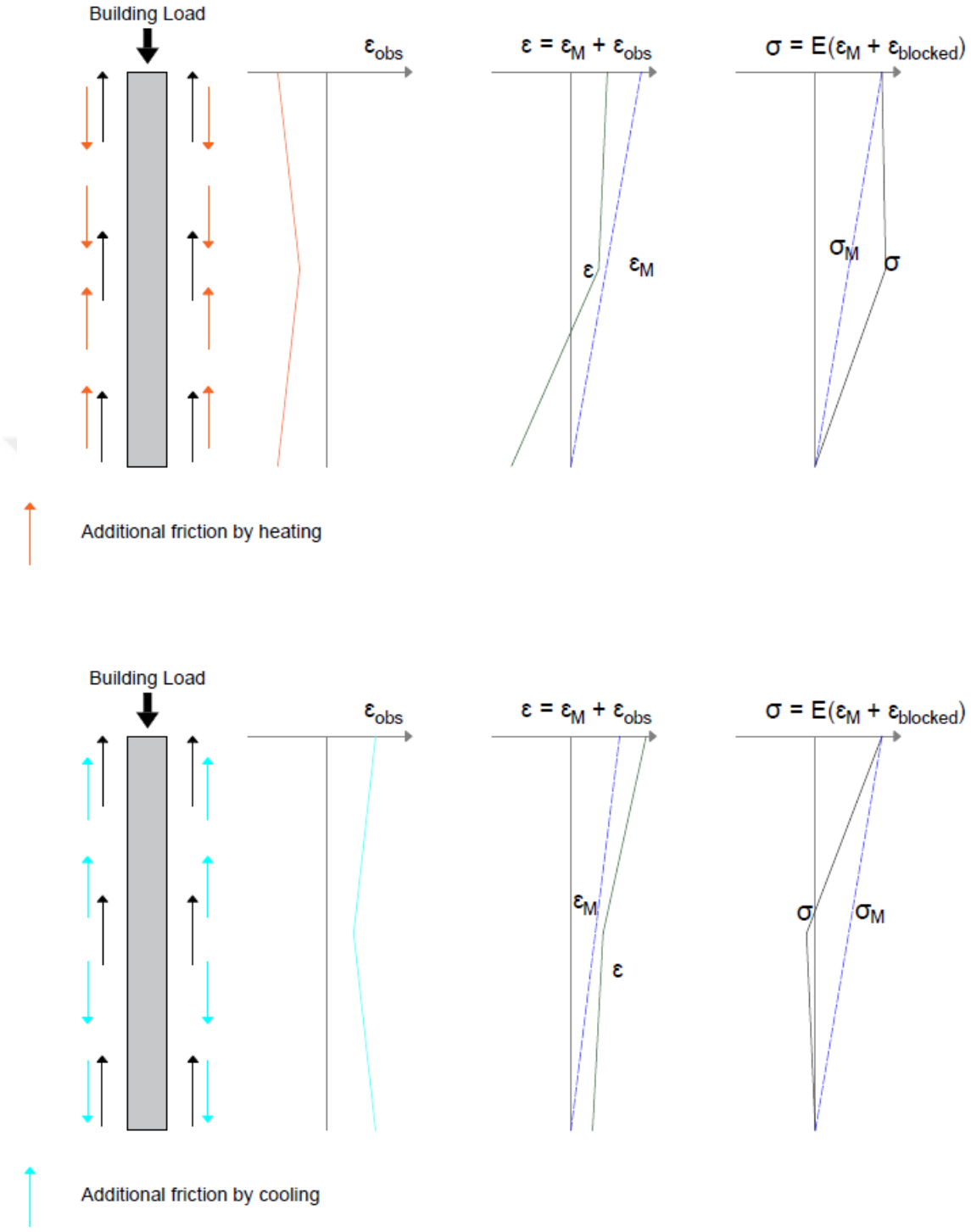


Figure 2.11. Thermo-mechanical behavior of a friction pile subjected to heating and cooling with mechanical load on top (modified after Soga and Rui, 2016).

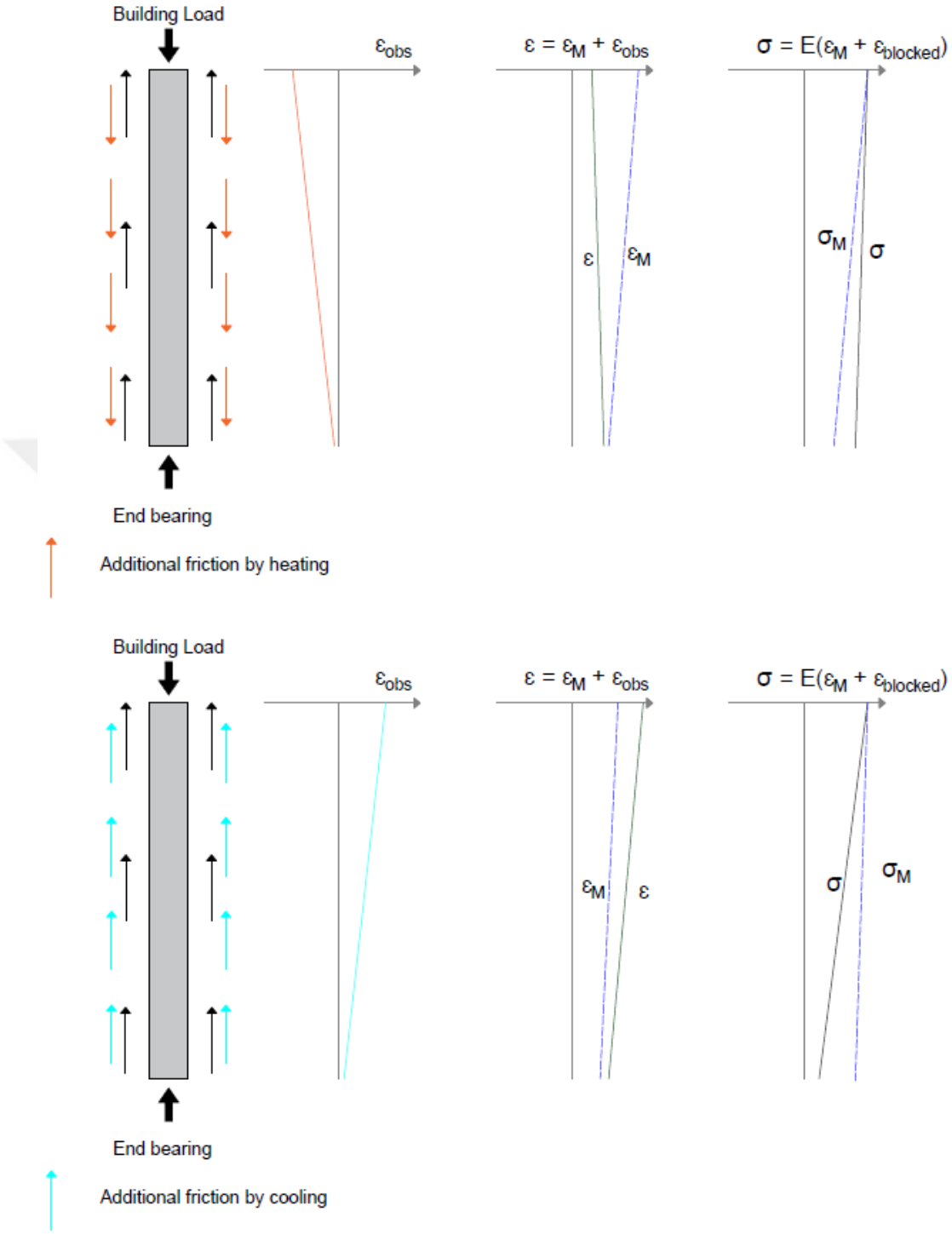


Figure 2.12. Thermo-mechanical behavior of an end-bearing pile subjected to heating and cooling with mechanical load on top (modified after Soga and Rui, 2016).

2.4.2. Modelling Approaches for Energy Piles

In numerical analyses, various techniques such as finite difference, finite element, and finite volume methods have been utilized. These techniques have been primarily employed within the thermo-mechanical modelling approach for energy piles (Moradshahi et al., 2021; Faizal et al., 2022; Heidari et al., 2022; Saggu and Sarma, 2023), with some applications also utilizing thermo-hydro-mechanical models (Sani et al., 2018; Sani and Singh, 2020; Behbehani and McCartney, 2022). Both modelling approaches are crucial depending on the specific conditions of the study. Thermo-mechanical models are simpler and suitable for scenarios where fluid flow is negligible, while thermo-hydro-mechanical models are more comprehensive and necessary for environments with significant water movement.

In numerical studies of energy piles conducted to date, researchers have predominantly assumed that surfaces are adiabatic, considered the initial ground temperature to be constant with depth, and modelled heat transfer below the ground solely through conduction while convection is considered in the heat exchanger fluid and at the interface with the inner surface of the pipes (Batini et al., 2015; Di Donna et al., 2016; Nguyen, 2017; Rotta Loria and Laloui, 2017; Moradshahi et al., 2022). A limited number of studies have taken atmospheric temperature variations into account, but only to a restricted extent. Some attempts have been made to indirectly represent atmospheric effects by imposing known temperature data along the depth of the ground and introducing additional Dirichlet boundary conditions at the ground surface (Caulk et al., 2016). Others have modelled atmospheric effects using heat flux solely from ambient temperature, excluding solar radiation and wind effects (Moradshahi et al., 2021, 2022; Faizal et al., 2022).

In terms of mechanical boundaries of the model, the sides of the ground are typically constrained to prevent horizontal movement, while the base is constrained to prevent both vertical and horizontal movement. The ground surface and the top of the pile can be modeled as fixed, pinned, or free, depending on whether a superstructure is present. Load applications at the pile head simulate structural loads transferred from the superstructure, which can be static or dynamic, representing different loading scenarios. For the pile-soil interface, either the load transfer method (Sutman, 2019; Ravera et al., 2020) or the rigid contact method

(Batini et al., 2015; Rotta Loria and Laloui, 2018; Heidari et al., 2022; Moradshahi et al., 2022) is commonly used, including in studies examining thermo-mechanical behavior.

Assumptions in mechanical modeling include the properties of materials and soils. Piles and soil layers are often assumed to be homogeneous and isotropic, meaning it has uniform properties in all directions, and soil profile may vary with depth and is modeled using stratified layers (Batini et al., 2015; Wu et al., 2021; Kong et al., 2023). The pile material is frequently assumed to behave in a linearly elastic manner under load, though plasticity models can be used for more detailed analyses (Knellwolf et al., 2011). Soil is typically modeled using elastic-plastic constitutive models to capture its nonlinear behavior under load (Saggu and Chakraborty, 2015; Garakani et al., 2021), although there are also studies where it is modeled as linear elastic (Wu et al., 2024). Thermal effects consider both the pile and soil undergoing thermal expansion, coupled with mechanical effects in the model, and the interaction between temperature changes and mechanical behavior is critical, especially for energy piles used for geothermal applications (Abdelaziz and Ozudogru, 2016).

2.5. Ground Heat Flow Mechanisms

Heat transfer involves the movement of energy between particles of matter that are at different temperatures. There are primarily three modes of heat transfer in soils: conduction, convection, and radiation. Although latent heat transfer can occur due to phase changes in material components, from an engineering perspective, this process is often considered insignificant when analyzing and designing energy geostructures (Xie and Qin, 2021).

2.5.1. Conduction

Conduction is a heat transfer mode that occurs at the molecular and atomic levels in solids and fluids with differing temperatures. Due to the predominance of lattice vibrations in the conduction process, this mode of heat transfer is more pronounced in solids compared to fluids. This process is generally invisible at a macroscopic level and relates to energy diffusion mechanisms. Conduction can be exemplified by the molecular movement within a

medium bounded by two surfaces at different temperatures, such as in an energy pile. Energy transfer occurs through continuous molecular collisions, moving from higher to lower temperature regions as per thermodynamic principles.

Conduction often dominates heat transfer in materials with pore sizes negligibly small relative to the solid volume such as soils and reinforced concrete. In reinforced concrete, conduction is the primary mode of heat transfer due to the characteristics of the concrete mix and the steel used in energy geostructures. Conduction also governs heat exchange across the thickness of pipes embedded in energy geostructures.

The conduction process follows Fourier's law, which states that the heat flux density (the rate of heat energy transferred per unit surface area per unit time) is governed by this law in a homogeneous and isotropic medium. Fourier's law is expressed as

$$Q = \lambda A \frac{dT}{dx} \tag{2.5}$$

where Q is the conductive heat flux, λ is the thermal conductivity of the material, A is the area of the material, and $\frac{dT}{dx}$ is the temperature gradient.

2.5.2. Convection

Convection is a form of heat transfer that takes place in fluids where there is a temperature difference. This process consists of two methods: energy transfer through diffusion, which involves the microscopic random movement of molecules similar to conduction, and bulk motion, which involves the macroscopic movement of fluid molecules collectively, also known as advection. When the fluid moves solely due to density changes caused by temperature differences, it is referred to as natural or free convection. If the movement is driven by other forces, it is known as forced convection.

Convection encompasses various flow regimes: internal flow, wherein the fluid is confined by surfaces such as within pipes; external flow, where the fluid moves over surfaces like atmospheric air over the ground; and seepage flow, in which the fluid permeates through porous materials, exemplified by groundwater movement through soil. For instance, when a fluid flows adjacent to a surface with a differing temperature, heat transfer occurs from the

surface to the fluid or vice versa, contingent upon the temperature gradient. At the interface, heat transfer predominantly occurs via molecular diffusion due to the negligible fluid velocity. Beyond this boundary layer, the bulk motion of the fluid substantially enhances the convective heat transfer process.

Newton's law of cooling describes the rate of convection, stating that the heat flux density is proportional to the temperature difference between the surface and the fluid, with the proportionality constant being the convection heat transfer coefficient

$$q_{conv} = h(T_s - T_f) \tag{2.6}$$

where q_{conv} is the convective heat flux, T_s is the temperature of the surface and, T_f is the temperature of the fluid.

2.5.3. Radiation

Radiation, such as electromagnetic waves, constitutes a form of heat transfer emitted by substances at any non-zero absolute temperature. This mode of energy transfer involves the propagation of thermal energy via electromagnetic waves through a medium or a vacuum. In solids and liquids, radiative heat transfer is generally minor compared to gases. The thermal energy emission stems from alterations in the electron configurations of the medium's atoms and molecules (Bergman et al., 2011).

The concept of radiation can be elucidated by analyzing the interaction between a medium at a specific temperature and a considerably larger surface at a different temperature. The radiation rate equation is governed by the Stefan-Boltzmann law. Heat flux density caused by solar radiation, the total radiosity X_r, consists of emitted and diffusively reflected radiation and defined as

$$\chi_r = \alpha_r G + \varepsilon_r B(T) FE(T) \tag{2.7}$$

where α_r, G, ε_r, B and $FE(T)$ are diffuse reflectivity, irradiation (total input radiative flux), emissivity, radiation power considering all wavelengths and fractional emissivity, respectively. Radiation power can be expressed by Stefan-Boltzmann law depending on varying temperature (T), Boltzmann constant σ_r and refractive index (r)

$$B(T) = r^2 \sigma_r T^4, \text{ and} \tag{2.8}$$

$$FE(T) = 0 \leq \frac{15}{\pi^4} \int_{\frac{C_2}{\lambda_{i-1}T}}^{\frac{C_2}{\lambda_i T}} \frac{x^3}{1-e^x} dx \leq 1 \tag{2.9}$$

where C_2, $\lambda_{i-1}$and λ_i are auxiliary radiation constant, wavelength at a given frequency (lower limit), wavelength at a given frequency (upper limit). The net inward radiative heat flux can be computed by subtracting irradiation and outgoing radiation including specular reflected radiation (s) from each other

$$q_r = G - (\chi_r + sG) = (1 - s)G - \chi_r \tag{2.10}$$

or

$$q_r = [1 - (\alpha_r + s)]G - \varepsilon_r B(T). \tag{2.11}$$

In conclusion, radiative heat transfer involves the emission and absorption of thermal energy through electromagnetic waves, as governed by the Stefan-Boltzmann law. This process is significantly influenced by surface characteristics such as emissivity and absorptivity.

3. FIELD TEST

3.1. Site Description

The details regarding the field test analyzed in this study were sourced from Sutman's research (Sutman, 2016). The experimental site is located in Houston, Texas, and consists of three test piles, three heat sink piles, and eight reaction piles, and boreholes as shown in the layout in Figure 3.1. The test piles were installed using the Continuous Flight Auger (CFA) cast-in-place method. Each pile has a diameter of 45.7 cm. Test Pile 1 (TP-1) and Test Pile 3 (TP-3) measure 15.24 m in length, while Test Pile 2 (TP-2) is 9.14 m long. For reinforcement, the test piles' rebar cage consists of four full-length vertical size 10 bars, evenly spaced, with size 22 steel bar rings positioned every 0.3 meters along the entire length of the 0.3-meter diameter cage. Additionally, a size 25 center bar extends the full length of the pile. The in-situ test setup utilized two water-to-water ground source heat pumps, each with a nominal capacity of 7 kW, and one of these heat pumps was directly connected to TP-1. This study focuses solely on the numerical modelling and comparative evaluation of TP-1. Figure 3.2 depicts the soil profile along the length of the test pile, and it predominantly consists of clay and sand layers, with the groundwater level approximately 3.7 meters below the surface.

Various field tests conducted, and correlations were employed to ascertain the thermal and mechanical properties of the soil layers and the pile. In-situ measurements targeted depths corresponding to three primary soil units: clay above the groundwater table, clay below the groundwater table, and sand below the groundwater table. Thermal parameters were derived from these field test results as bulk values (Brettmann and Amis, 2011; Sutman, 2016; Sutman et al., 2019). Table 3.1 provides a detailed overview of the parameters for the soil layers, energy pile, and the pipe within the piles.

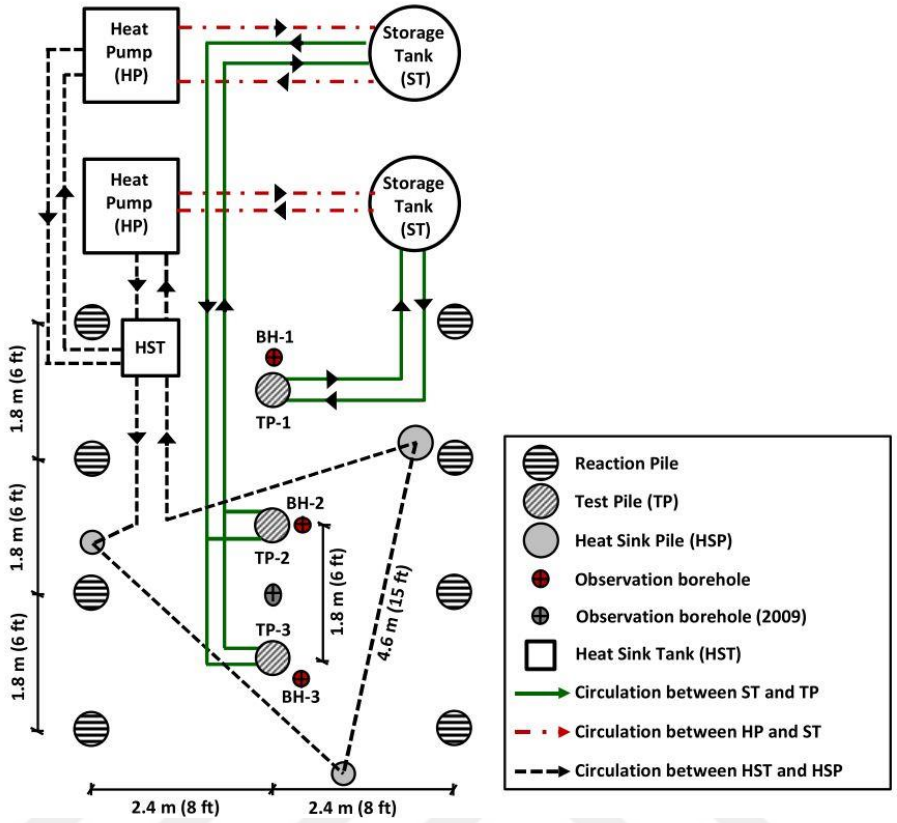


Figure 3.1. Layout of experimental site in Houston, Texas (Sutman, 2016).

Table 3.1. Thermal and mechanical properties of soil layers, pile and pipes.

Properties	**Clay**	**Sand**	**Pile**	**PEX pipes**
Elastic modulus, E (MPa)	45	75	36000	-
Poisson's ratio, ν (-)	0.495	0.30	0.18	
Unit weight, γ (kN/m^3)	2005	1986	2044	-
Volumetric heat capacity, C (MJ/m^3°C)	2.61	2.61	1.80	-
Thermal conductivity, λ (W/m°C)	2.1	1	2	0.42
Thermal expansion coefficient, α (με/°C)	1.5	1	12.9	-

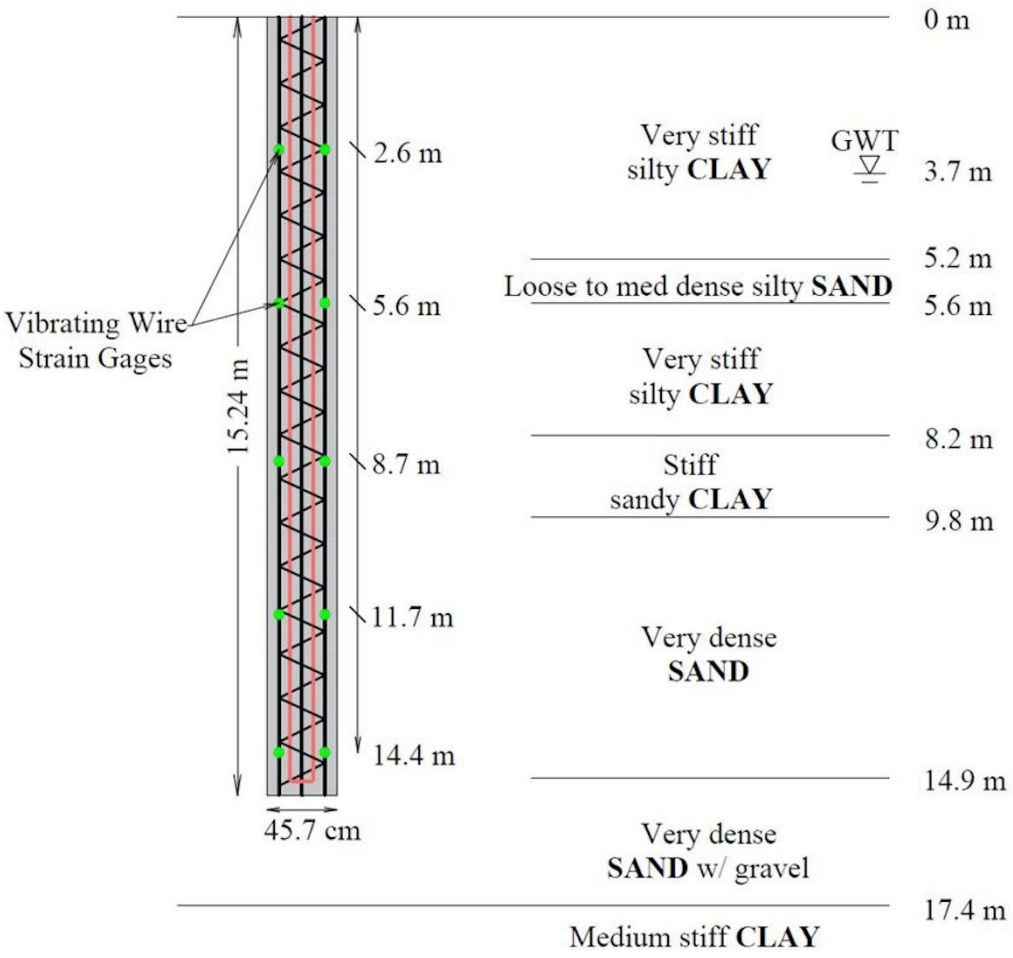


Figure 3.2. Pile and soil profile (modified after Sutman et al., 2019).

3.2. Instrumentation

For the heating and cooling system within the test pile, a single U-shaped polyethylene (PEX) pipe with a nominal diameter of 25.4 mm and a wall thickness of 3.2 mm was used. The spacing between these pipes varies in some sections due to construction factors, averaging around 6.4 cm, as illustrated in Figure 3.3. The energy pile's instrumentation configuration is shown in Figure 3.4. Five pairs of Vibrating Wire Strain Gages (VWSGs) were strategically placed at different depths along the pile length to measure both strain and temperature, as seen in Figure 3.2.



Figure 3.3. Arrangement of the sensors and pipes within the pile (Sutman, 2016).

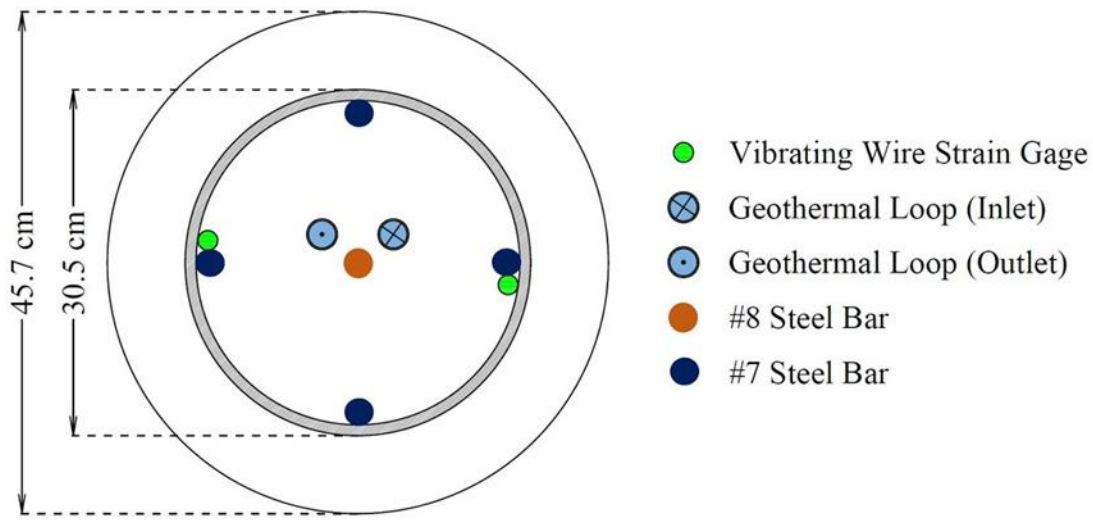


Figure 3.4. Cross-sectional layout of the sensors within the pile (modified after Sutman et al., 2019).

3.3. Schedule of In-Situ Tests

Two types of in-situ test procedures were carried out in the mentioned study. The first test aimed to examine the response of an energy pile to multiple cyclic thermal loads without a maintained mechanical load, applied to TP-1. For this in-situ test, TP-1 was initially loaded to its ultimate capacity of 2558 kN, before the application of thermal cycles. Then, the test pile was subjected to multiple cyclic thermal loads without the imposition of a mechanical load. Over a six-week period, a total of five thermal cycles were applied, as illustrated in Figure 3.5. The temperature of the heat exchanger fluid which consisted of 80% water and 20% antifreeze (ethylene glycol), was adjusted daily, increasing or decreasing by 10°C, with a maximum temperature of 43°C and a minimum of 8°C. Upon completion of the thermal cycles, the test pile was reloaded to 2558 kN (Sutman, 2016).

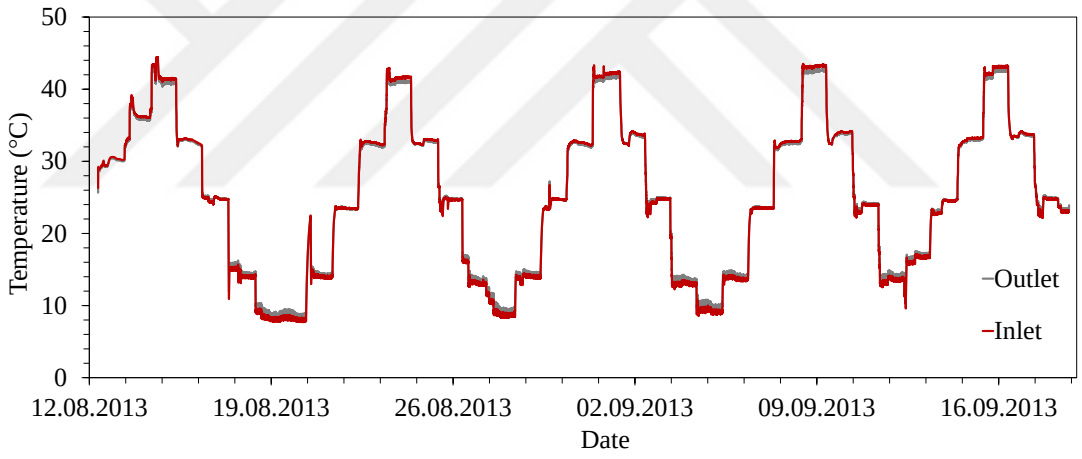


Figure 3.5. Thermal loads applied to the pile (modified after Sutman et al., 2019).

3.4. Test Results

The temperature profiles obtained along the pile during the first heating-cooling episode are presented in Figure 3.6. The temperature data shown were obtained just before the change in inlet fluid temperature to represent the highest temperature variation over the days.

The strain data along the test pile were recorded by VWSGs, which were also exposed to temperature changes during the field test. These data include observed strains. Blocked

strains are needed to calculate thermally induced axial stresses. As described previously, blocked strains and thermally induced axial stress data were obtained by calculating the theoretical strain that would occur if the piles were free of constraints, and then taking the difference between this theoretical strain and the observed strains measured by the VWSG sensors. The thermally induced axial stresses along the pile for the first heating-cooling episode, obtained through the calibration of the specified data, are presented in the Figure 3.7.

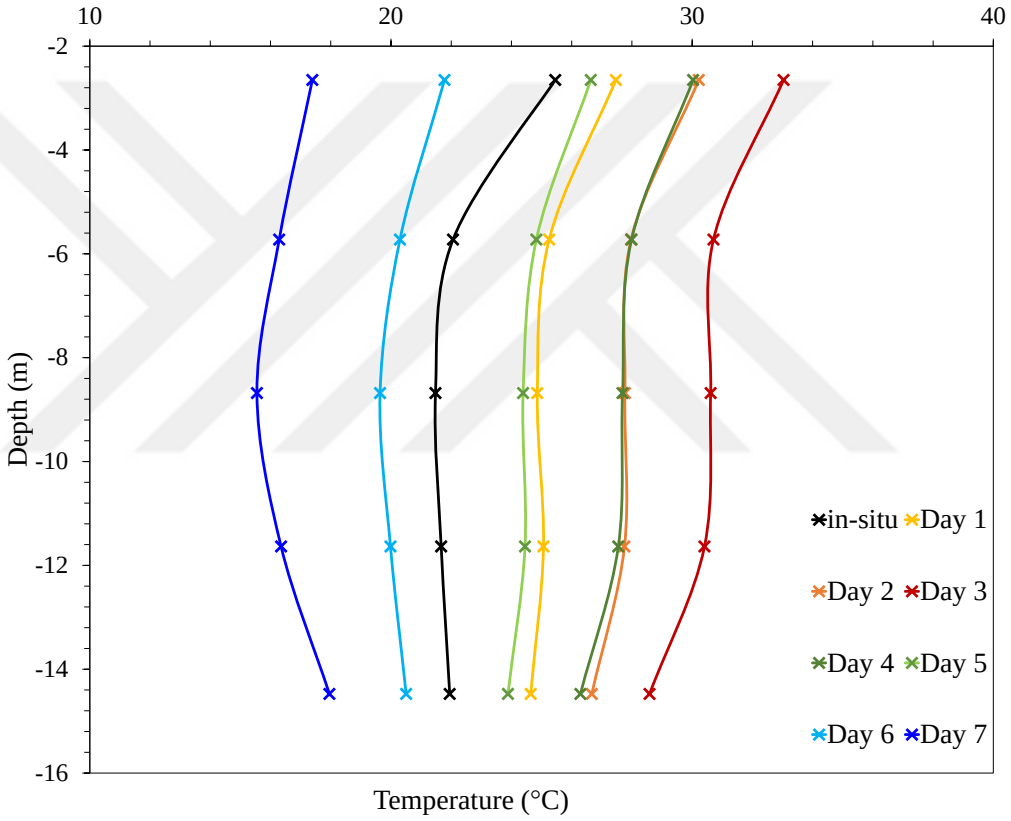


Figure 3.6. Temperature profiles along the pile during the first episode of heating and cooling (modified after Sutman et al., 2019).

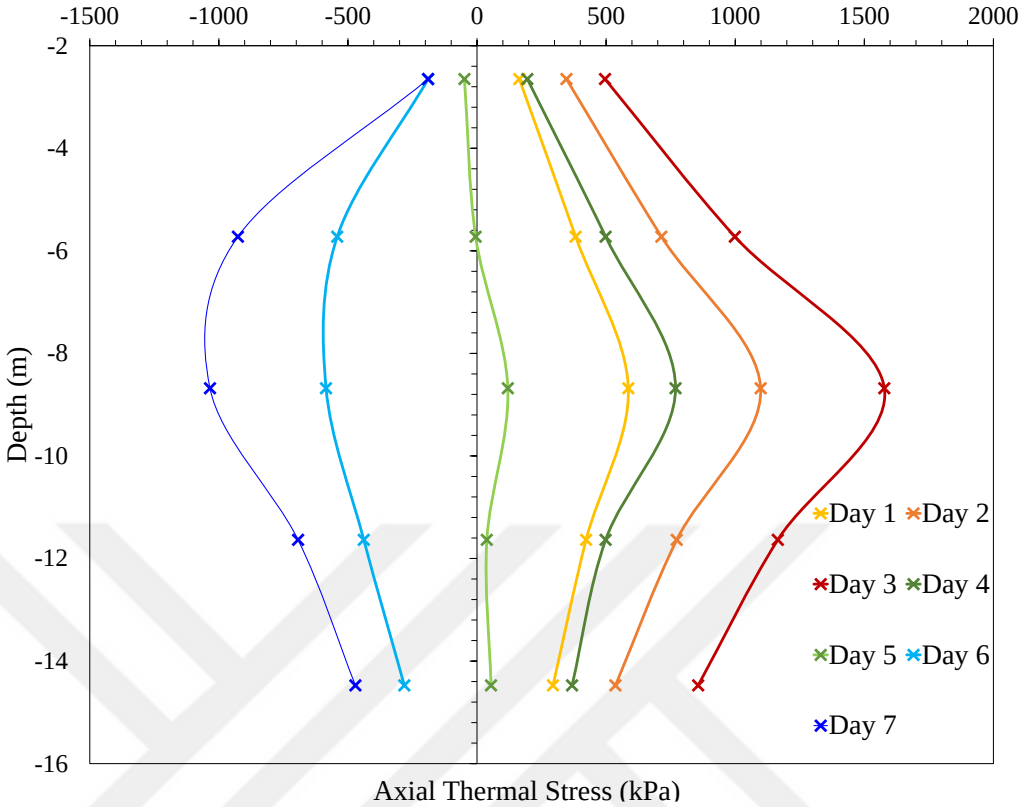


Figure 3.7. Thermally induced axial stresses along the pile during the first episode of heating and cooling (modified after Sutman et al., 2019).

4. NUMERICAL MODEL

4.1. Description of The Model

To model the field experiment conducted on TP-1 and to reproduce the thermal and thermo-mechanical responses, COMSOL Multiphysics Software was employed. This software is capable of performing numerical simulations using three-dimensional finite elements and supports multiphysics, making it the preferred choice for scenarios involving multiple physical phenomena. For this numerical study, four main physics interfaces and two multiphysics couplings were utilized:

- Heat Transfer in Porous Media: To model heat transfer in the pile and soil.
- Heat Transfer in Pipes: To model the heat exchanger fluid.
- Solid Mechanics: To reproduce the mechanical response in the pile and soil.
- Surface-to-Surface Radiation: To simulate surface solar radiation.
- Thermal Expansion: Coupling heat transfer in porous media and solid mechanics to model the thermo-mechanical behavior in both the pile and the soil.
- Heat Transfer with Surface-to-Surface Radiation: To account for heat transfer due to solar radiation from the surface.

4.2. Model Geometry

The model represents a block that is 40 m long, 50 m high, and 50 m deep, which simulates the soil. An energy pile is located in the center of the block. The geometries of both the pile and the soil were based on actual field conditions. The energy pile is 15.24 m long with a diameter of 45.7 cm. The soil profile was conceptualized with three layers based on the stratigraphy determined during fieldwork and subsequent laboratory sampling: clay above the water table, and clay and sand below the water table. To avoid boundary effects, lateral boundaries were set approximately 25 meters from the pile surface. The overall view of the model is presented in the Figure 4.1.

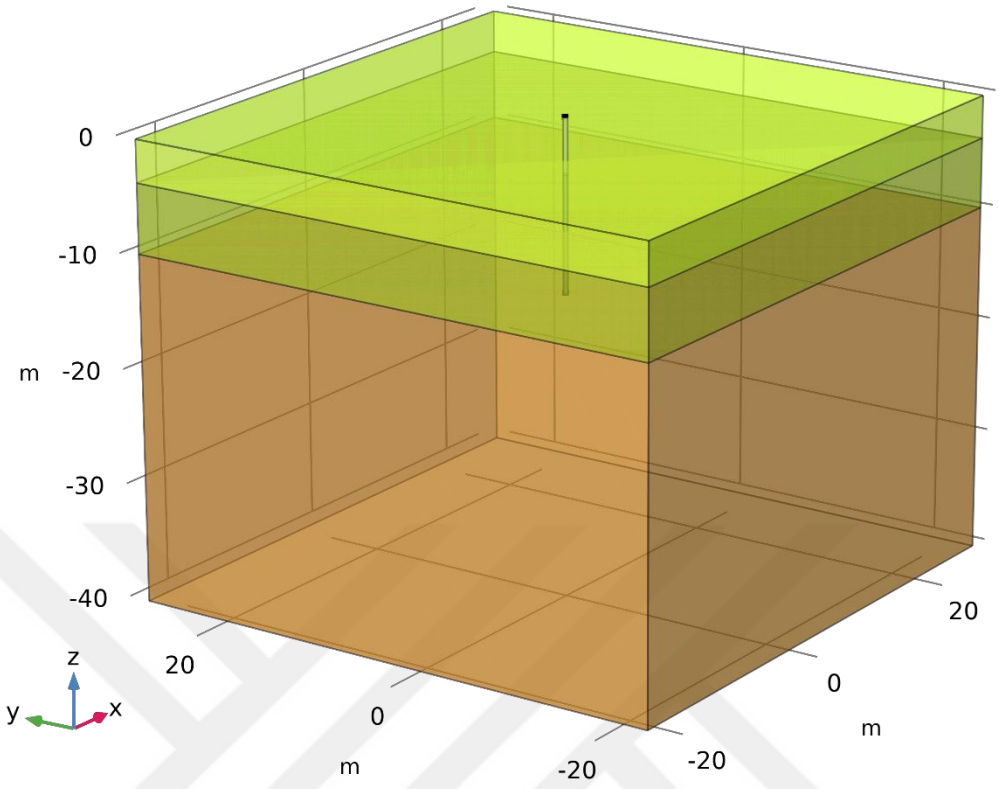


Figure 4.1. 3D view of the model.

The energy pile and the soil were assumed to be bonded, with no specific interface elements at their junction. This approach follows established practices commonly observed in previous studies on the thermomechanical behavior of energy piles (Batini et al., 2015; Rotta Loria and Laloui, 2018; Heidari et al., 2022; Moradshahi et al., 2022).

The pipes within the pile were represented as line elements. Two linear lines and a curve for the pipe turning point were created within the pile using parametric curve selection. The line elements are shown in the Figure 4.2. For computational convenience, The Heat Transfer in Pipes module includes the pipes as line elements in the geometry, and later incorporates inputs for the pipe geometry within the module. The inner diameter was defined as 19 mm and the wall thickness as 3.2 mm in the module.

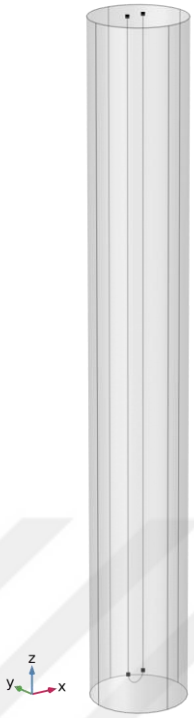


Figure 4.2. 3D view of the pile and line elements that represent pipes.

4.3. Modelling Assumptions

Various assumptions were made in developing the numerical model. The soil and the pile were modelled as a porous medium made up of solid particles with voids filled with air and/or water. The energy pile was assumed to be an isotropic linear elastic material. The inertial effects of the solid skeleton were considered negligible since the simulations represented quasi-static conditions with gradually applied loads. The Mohr-Coulomb material model was used for the soil layers. Radial displacements and their impacts on soil response were ignored, as they were assumed to be minor compared to axial displacements. Additionally, it was assumed that the properties of both the soil and the pile were not affected by temperature changes. A thermal expansion multiphysics coupling node was employed to calculate the constrained thermal strains within the pile due to temperature variations and the resulting axial stresses. In the pipes, the heat carrier fluid was composed of 80% water and 20% antifreeze (ethylene glycol) to replicate the field test conditions. The thermal and mechanical properties of the soil layers, energy pile, and PEX pipes were sourced from previous studies conducted at the site as detailed in Table 3.1.

4.4. Governing Equations

To precisely simulate the thermo-mechanical behavior of energy piles, a thermo-mechanical formulation is used. This formulation is applied through the use of COMSOL Multiphysics to develop time-dependent, thermo-mechanical finite element models. The model incorporates a mechanical equilibrium equation

$$\nabla \cdot \sigma_{ij} + F_v = 0 \tag{4.1}$$

where ∇ denotes the divergence, σ_{ij} represents the total stress tensor, and F_v is the volume force factor. To account for the impact of thermal loading on the energy pile, the total stress tensor is calculated as

$$\sigma_{ij} = D_{ijkl}(d\varepsilon_{kl} - \beta_{kl} dT) \tag{4.2}$$

where $D_{ijkl}$is the elastic stiffness tensor, ε_{kl} is the total strain tensor, β_{kl} is a vector that includes the linear thermal expansion coefficient of the material, and T is the temperature.

The heat transfer mechanism considered for the soil layers for this field test was thermal conduction. By excluding thermal convection, the heat transfer equation governing the interaction between the heat exchanger fluid, pipe walls, and the external ground can be derived as

$$\rho C \frac{\partial T}{\partial t} + \nabla \cdot (Q + q_r + q_w) = 0 \tag{4.3}$$

where ρ, C, T, t, Q, q_r and q_w denote material density, specific heat capacities of water and solid materials, temperature, time, heat flux for conduction, net inward radiative heat flux, and the convective heat flux caused by wind, respectively. In Equation (4.3), the first term represents the internal stored energy for the soil and pile, while the second term embodies conduction heat transfer as described by Fourier's law.

The energy conservation equation for the liquid flowing through the pipes can be formulated as

$$\rho_l A_p C_l \frac{\partial T_l}{\partial t} + \rho_l A_p C_l u_l \cdot \nabla T_l - \nabla \cdot \left[A_p \lambda_l \nabla (T_l)\right] - Q_{wall} = 0 \tag{4.4}$$

where ρ_l, C_l, A_p, T_l, u_l and λ_l are density, specific heat, pipe cross sectional area, temperature, velocity and thermal conductivity of the circulating liquid through pipe, respectively. Q_{wall} is the heat flux per unit pipe length, and it is expressed as

$$Q_{wall} = h_{eff}(T_{ext} - T_l) \tag{4.5}$$

where h_{eff} is a coefficient of the circular shaped pipe wetted perimeter for the heat transfer and T_{ext} is the temperature of the outer surface of the pipe. Pipe heat transfer coefficient can be obtained as

$$h_{eff} = \frac{2\pi r_{int}}{\frac{r_{int}}{\lambda_p}\ln\left(\frac{r_{ext}}{r_{int}}\right)+\frac{1}{h_{int}}} \tag{4.6}$$

where r_{int}, r_{ext}, λ_p and h_{int} are internal pipe radius, external pipe radius, thermal conductivity of the pipe and h_{int} is the coefficient for convective heat transfer of the internal surface of the pipe, respectively. The latter term depends on the pipe and liquid properties and calculated as

$$h_{int} = \frac{Nu\lambda_l}{\frac{4A}{2\pi r_{int}}}, \tag{4.7}$$

$$Nu = \max(3.66; Nu_{turbulent}), \tag{4.8}$$

$$Nu_{turbulent} = \frac{\left(\frac{f_d}{8}\right)\left(\frac{\rho u_l r_{int}}{\mu}-1000\right)\left(\frac{\mu C_l}{\lambda_l}\right)}{1+12.7\sqrt{\frac{f_d}{8}}\left[\left(\frac{\mu C_l}{\lambda_l}\right)^{\frac{2}{3}}-1\right]}, \text{ and} \tag{4.9}$$

$$f_d = \left[-1.8\log\left(\frac{6.9}{\frac{\rho u_l r_{int}}{\mu}}\right)\right]^{-1} \tag{4.10}$$

where $Nu_{turbulent}$, f_d, μ, u_l, C_l and λ_l and are Nusselt number for turbulent flow in pipes, coefficient of friction, liquid dynamic viscosity, velocity of fluid, liquid specific heat and thermal conductivity of the liquid, respectively.

The heat exchange between the ground and atmosphere is the combination of solar radiation and wind convection. The equations for the net inward heat flux density due to solar radiation are described in Chapter 2.5.3. Convective heat flux caused by wind is expressed as

$$q_w = h\left(T_f - T_s\right) \tag{4.11}$$

where h, T_f and T_s are heat transfer coefficient of air, ambient temperature, and temperature of the ground surface, respectively.

4.5. Boundary and Initial Conditions

Figure 4.3 illustrates the mechanical boundary conditions. The model's base was subjected to a fixed boundary condition, fully constraining both vertical and horizontal displacements. Roller boundary conditions were applied along the model's lateral boundaries to restrict horizontal movement, while the upper boundary was left free. Initial stress states due to gravity were assumed to be geostatic for the soil and isotropic for the pile.

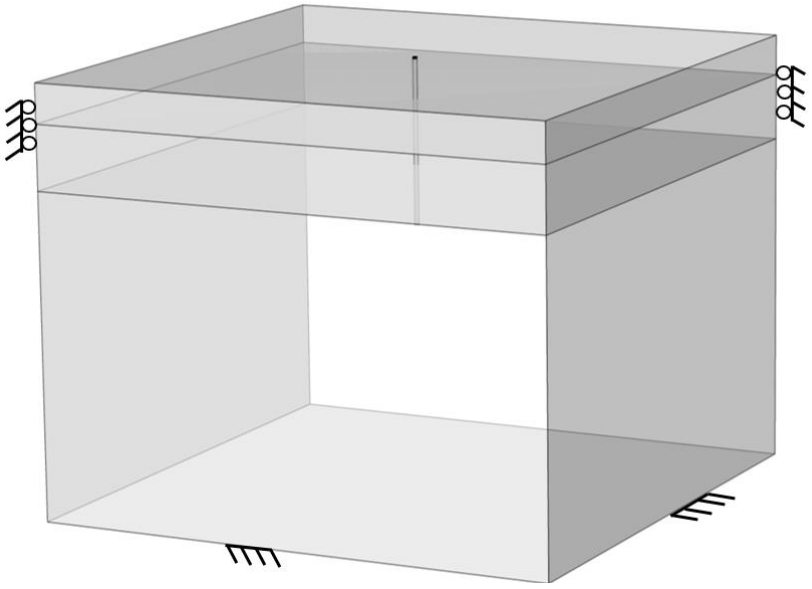


Figure 4.3. Mechanical boundary conditions applied to the model.

Thermal boundary conditions included thermal insulation on the sides and bottom of the model, with solar radiation and air convection allowed on the upper surface. The initial temperature of both the soil and the pile was set at 21.6°C, based on initial field temperature readings taken alongside the pile.

In the simulations, the temperature recorded at the pipe inlet during the field test consistently represented the circulation of the heat carrier fluid within the pipes. Figure 3.5 shows the inlet temperature of the heat carrier fluid as incorporated into the numerical model. Figure 4.4 demonstrates that the comparative analysis between the measured outlet

temperature of the heat carrier fluid and the simulated results shows significant agreement, accurately reflecting the field conditions.

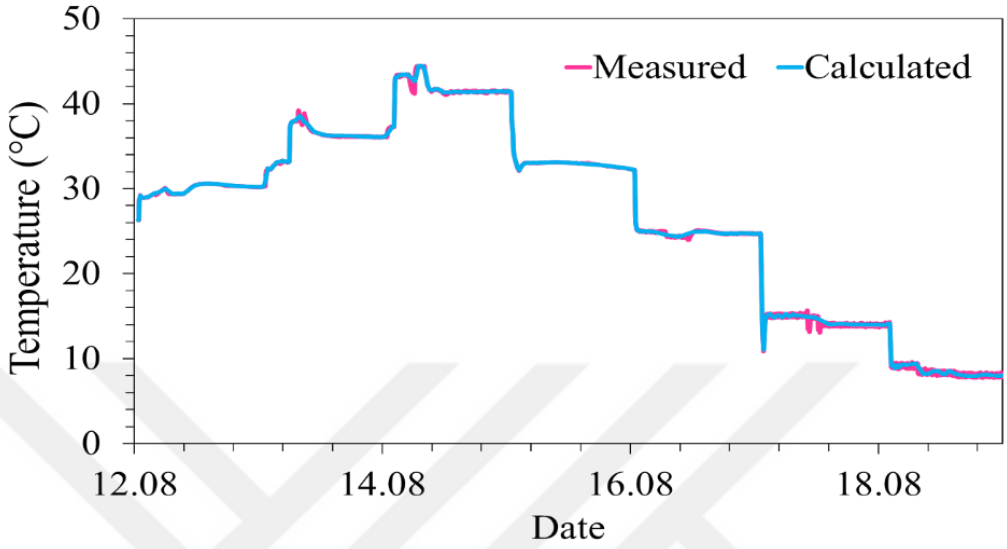


Figure 4.4. Comparison of measured and calculated outlet temperatures.

4.6. Mesh

The mesh included 106,809 elements, consisting of tetrahedral, triangular, prismatic, linear, and vertex elements, with 27,668 mesh elements specifically representing the pile. To ensure the accuracy of this mesh, an evaluation of the mesh element quality was performed. The general view of the mesh can be seen in Figure 4.5.

To ensure the validity of a model, the quality of the mesh elements must be assessed. Table 4.1 outlines three criteria used to measure mesh quality, as specified by COMSOL. These criteria are scored between 0 and 1, with a score of 1 indicating a high-quality mesh. Poor-quality mesh elements can result in convergence issues and inaccurate outcomes.

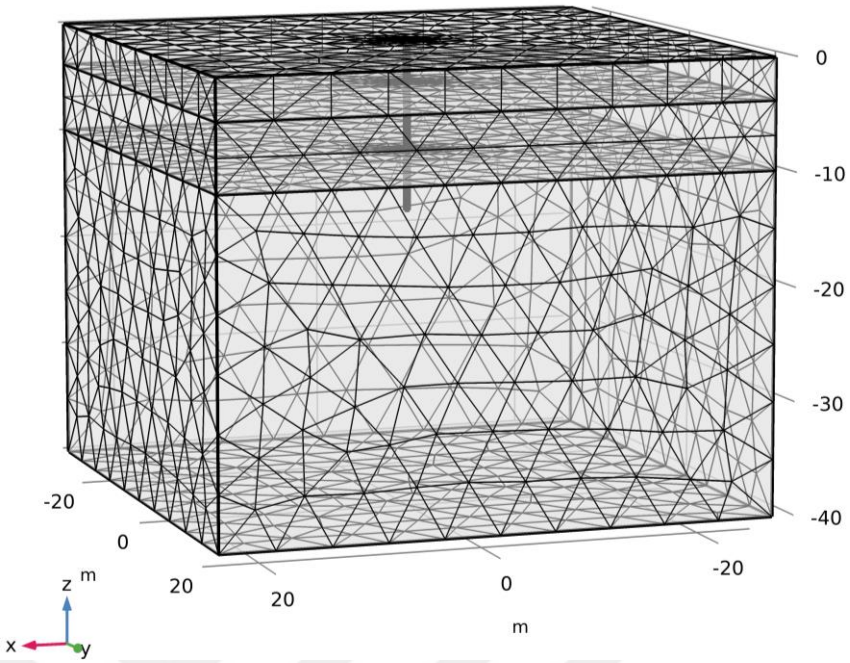


Figure 4.5. General view of the mesh applied to the model.

4.6.1. Skewness

This criterion measures the angle between two edges of an element compared to the corresponding angle in an ideal element. The average skewness value indicates whether the mesh quality is acceptable. In general, elements with a quality below 0.1 are considered poor quality for many applications. The formula used is

$$1 - max\left(\frac{\theta-\theta_e}{180-\theta_e}, \frac{\theta_e-\theta}{\theta_e}\right) \tag{4.12}$$

where θ represents the angle over an edge and θ_e is the angle of the corresponding edge in an ideal element.

4.6.2. Maximum Angle

This criterion evaluates the largest angle within an element. If this angle is smaller than the largest angle in the ideal element, the quality score is 1. Otherwise, the quality score reflects how much larger this angle is compared to the ideal element, indicating the mesh quality.

4.6.3. Growth Rate

This criterion measures local anisotropic growth rates, comparing the maximum and minimum growth rates of an element to its neighboring elements. A value of 1 indicates uniform growth in all directions, signifying no anisotropy. The formula used is

$$\frac{\min(s(e),s(e_a))}{\max(s(e),s(e_a))} \tag{4.13}$$

where $s(e)$ is the area of an element e and $s(e_a)$ is the area of a neighbor element in the spatial direction a.

Table 4.1. Summary of mesh element quality.

	Minimum Element Quality	**Average Element Quality**
Skewness	0.1384	0.6345
Maximum Angle	0.2071	0.7027
Growth Rate	2005	0.738

4.7. Model Development

4.7.1. The Positioning of The Sensors

The positioning of sensors is a crucial factor influencing the compatibility of the temperature and stress outputs between the model and the field test measurements. Although the axial positions of the sensors for TP-1 are specified (Sutman et al., 2019), their precise placements within the pile cross-section remain uncertain due to construction variability. Therefore, the aim is to establish a reasonable distance range from the pile axis for output locations in the analysis. According to Sutman et al. (2019), the sensors are attached to the vertical reinforcement, as illustrated in Figure 3.3. Considering the diameter and thickness of the vertical reinforcement at the cross-section and potential location variations due to the pile construction technique, it was determined that the sensors could be situated within a distance range of 11.7 to 12.9 cm from the pile center. Assuming this range includes the zone where the VWSG sensors were located during the field test, temperature and stress data from this specified area are collected in the finite element analysis (D=11.7 cm to D=12.9 cm). In the remainder of this study, these distances will be denoted by the symbol "D".

4.7.2. Incorporation of Solar Radiation and Wind Convection

Field measurements of undisturbed temperature at various depths along the pile prior to activation indicated that the temperature varied within the first six meters but remained constant beyond that depth. This temperature variation within the first six meters is attributed to the influences of air temperature and surface radiation. To accurately simulate the initial temperatures of the site, ambient environmental characteristics from the two months leading up to and during the field test (see Figure 4.6) were applied to the model. For this purpose, meteorological data from 2013, sourced from the Houston William P. Hobby weather station located approximately 45 km away, was utilized. The heat transfer module employed a dataset from ASHRAE Data Viewer 5.0 (ASHRAE, 2013), which includes detailed information on temperature, dew point, wind speed, air pressure, and solar radiation, specific to calendar days and times for that location. Surface-to-surface radiation was included in the model to gradually match the initial undisturbed field temperature.

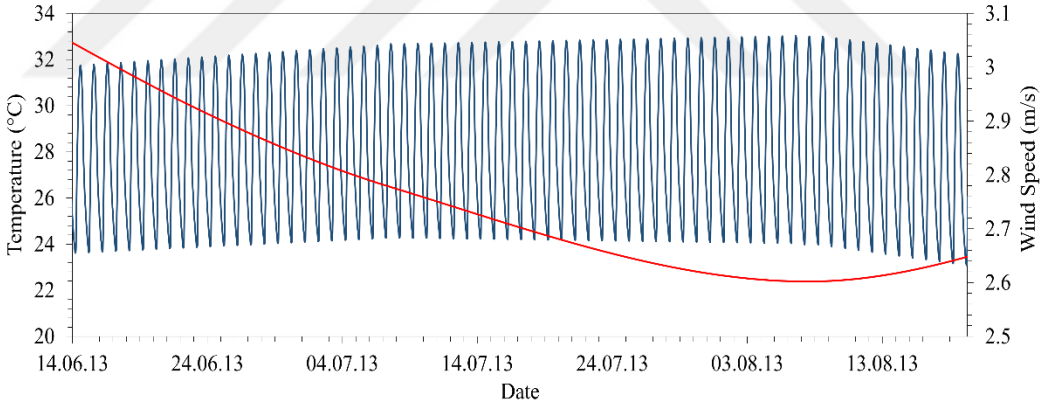


Figure 4.6. Ambient temperatures and wind speed for the two months preceding and during the field test at William P. Hobby weather station (ASHRAE, 2013).

In addition to solar radiation, wind affects surface temperatures in exposed environments, causing both free and forced heat convection from all exposed surfaces to the ambient air. To represent this effect in the analysis, a convective heat flux was applied to the surface. The external temperature required for this simulation feature was derived from the weather station data, and the heat transfer coefficient, which depends on wind speed and

air properties, was calculated using a specific relation developed by Rao (2004) for low wind speeds below 4 m/s, as these were the prevailing wind conditions at the field site

$$h = 0.025\rho_a C_{p,a} v_a^{0.3} \quad (4.14)$$

where ρ_a and $C_{p,a}$are density and specific heat capacity of air, respectively and va represent wind velocity.

4.7.3. Pre-Analysis Evaluation: With and Without Solar Radiation and Wind

Figure 4.7 compare initial field temperatures from simulations that include and exclude the effects of solar radiation and wind. Figure 4.8 present simulation results for two sensor locations on the first day of heating, considering both solar radiation and wind, as well as simulations excluding these factors. The findings reveal that both the initial measurements before thermal activation and the first day's heating results accurately represent temperature fluctuations within the first six meters of the pile in the model that includes solar radiation and wind effects. Additionally, Figure 4.9 compare simulation results for the first day of heating, incorporating both radiation and wind effects, with simulations that exclude these factors. The evaluation of stresses indicated that simulations accounting for radiation and wind effects produced temperature-induced stresses that are closer to actual field conditions. Given the better alignment of these results with field conditions, the model incorporating solar radiation and wind effects was used for the subsequent analyses presented in the following section.

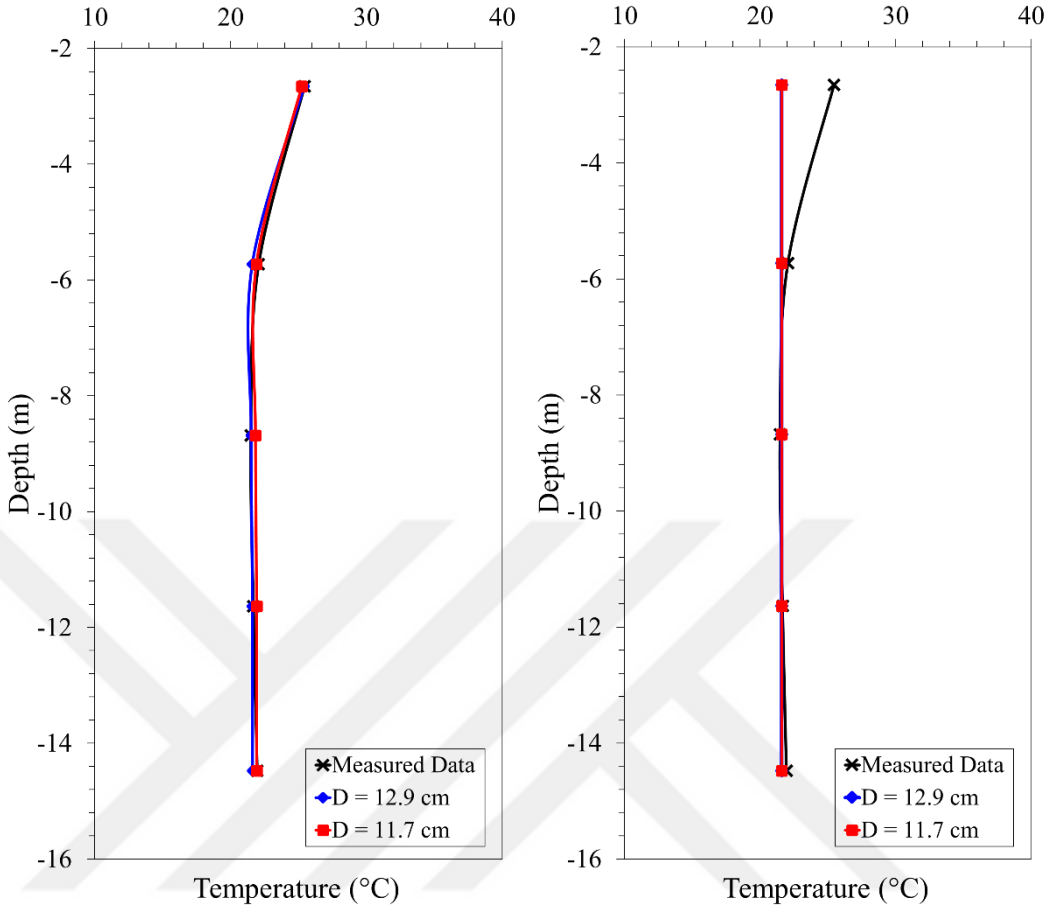


Figure 4.7. Initial field temperatures prior to the test obtained by simulations (a) with solar radiation and wind effects, (b) without the solar radiation and wind effects.

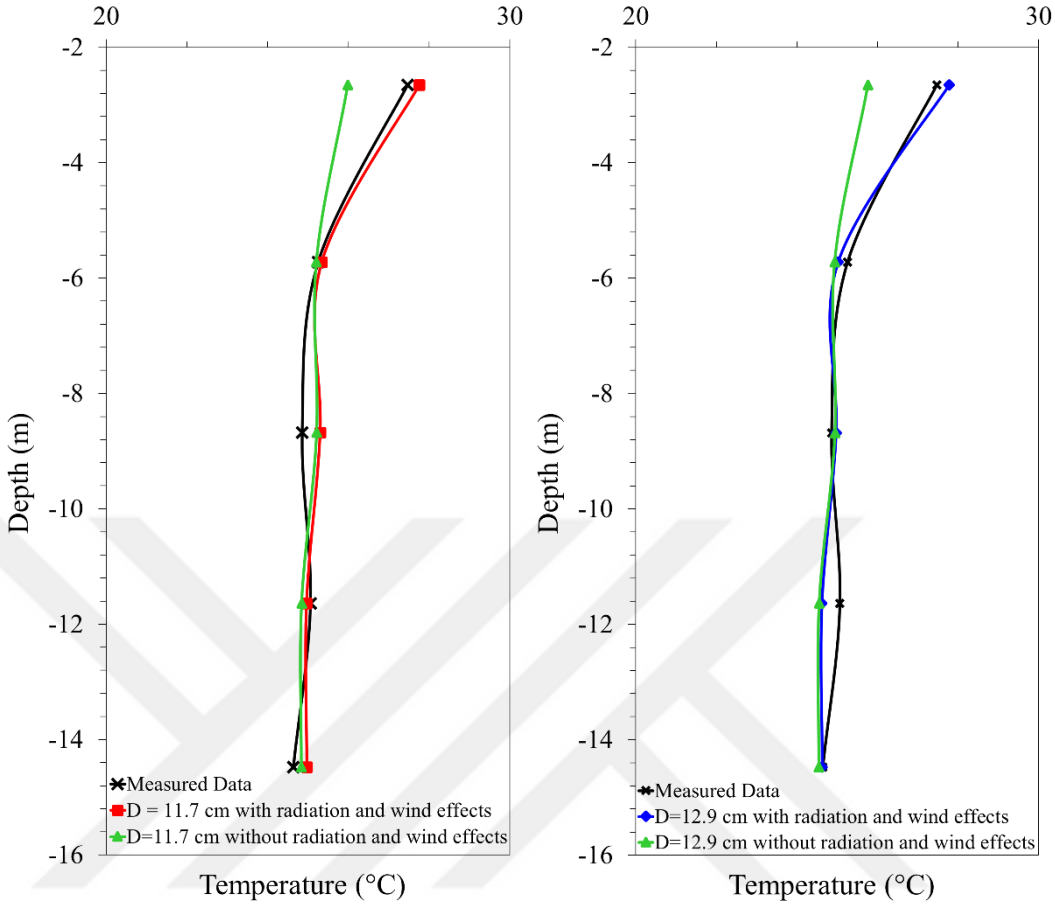


Figure 4.8. Temperature measurements on the 1st day of heating from simulations with and without solar radiation and wind effects: (a) at D=11.7 cm, (b) at D= 12.9 cm.

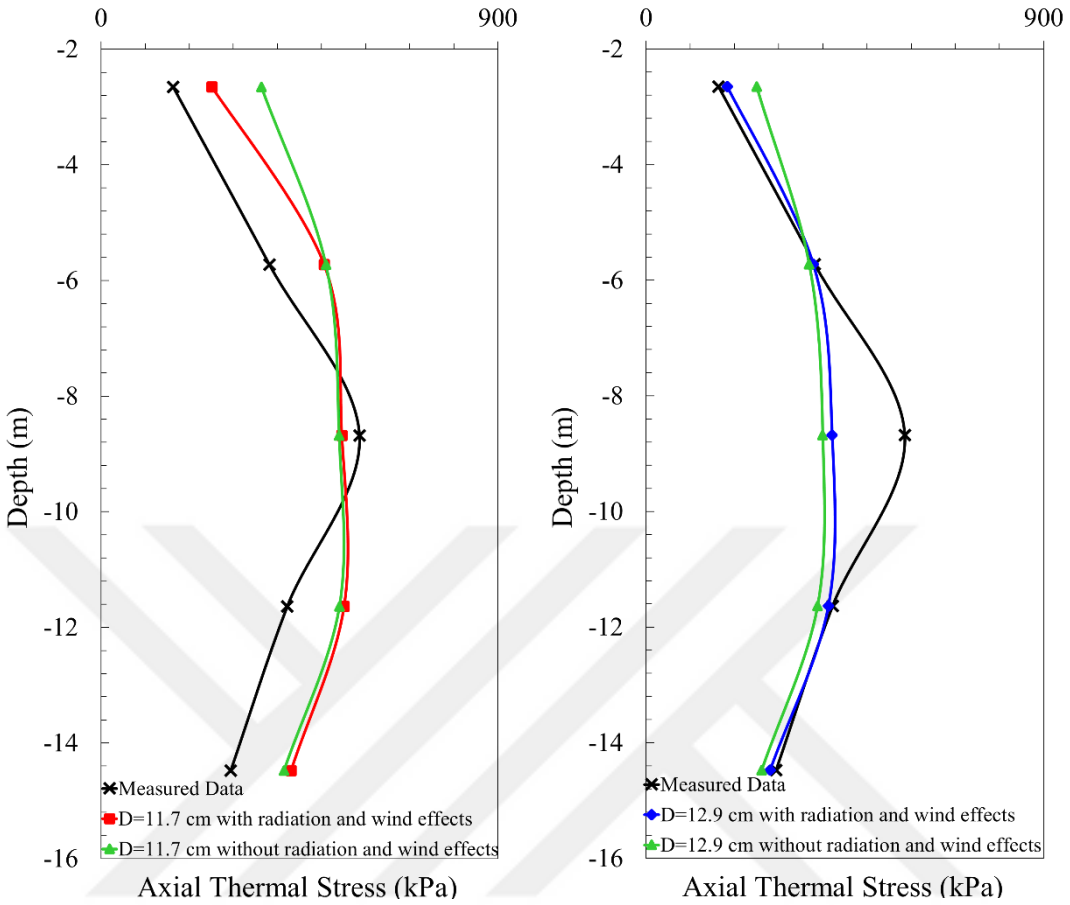


Figure 4.9. Thermally induced axial stress measurements on the 1st day of heating from simulations with and without solar radiation and wind effects: (a) at D=11.7 cm, (b) at D= 12.9 cm.

5. FIELD RESULTS AND NUMERICAL VALIDATION

Figures 5.1 to 5.7 illustrate the axial stresses and temperatures induced by thermal effects along the pile during the initial heating and cooling cycle. The numerical analyses incorporate surface solar radiation and wind convection from the start to simulate the field temperatures along the pile's length during thermal loading. At the site, the initial soil temperature before the test was recorded at 25.5°C by the Vibrating Wire Strain Gages (VWSGs) at a depth of 2.7 meters, which then gradually decreased to 21.5°C and remained stable beyond approximately 6 meters. The atmospheric conditions significantly affected the soil temperature above the 6-meter depth. The temperature reduction was attributed to solar radiation at the ground surface, combined with wind effects, as described by Brandl (2006). The numerical analyses closely matched this phenomenon, with a deviation of ±0.3°C from the observed data.

Upon heating, the temperatures along the pile increased as expected. During the heating period, the pipe inlet temperature was gradually raised to 45°C over three days (Figure 3.5), resulting in a measured pile temperature of 31.5°C at a depth of 2.7 meters. The temperature rise was non-uniform, with the highest increase (9.1°C) occurring in the mid-section and upper part of the pile, while the bottom part experienced a smaller rise (6.6°C), as shown in Figure 5.3. Numerical analyses provided corresponding values of 9.0~9.4°C for the maximum increase and 7.4~7.8°C for the minimum increase. The difference between measured and computed temperatures was less than 1.0°C, indicating that the numerical model accurately reflects the overall behavior of the thermally loaded pile. Despite the consistent daily increment applied to the inlet temperature during the heating period, the temperature rise along the pile depth was inconsistent. The maximum increase between successive days varied from 3.3°C to 3.5°C, occurring in the mid-section and top part of the pile. The minimum increase, occurring at the bottom of the pile, ranged from 2.1°C to 2.6°C. The non-uniform temperature rise along the pile is attributed to varying heat gradients throughout the pile. The proximity of the top of the pile to the heat source causes the fluid to circulate at higher temperatures compared to the tip of the pile, resulting in a high temperature gradient and greater heat exchange between the pile and the soil. As the heat-

carrying fluid moves downward, its heat flux decreases, leading to a smaller increase in pile temperature.

Figures 5.1 to 5.7 show the axial stress values, with observed temperature changes explaining the development of thermally induced axial stresses. These stresses were determined by subtracting the in-situ stresses before thermal activation from those observed after activation. The sign convention assumes compression as positive. During heating, compressive stresses increased, with the most significant change occurring at around 8.7 meters depth. This is due to the pile's restraining conditions, which allow free upward deformation due to the lack of structural load and partially restrained downward deformation due to toe resistance. Consequently, the stress increase distribution was asymmetrical along the pile relative to its mid-section. Field measurements indicated that the axial stress at the pile's midsection rose to approximately 1600 kPa by the last day of heating (day 3), while numerical analysis computed it at 1400 kPa. The least thermally induced stress increase during heating was measured at 500 kPa at the top of the pile, with numerical analyses computing it between 550 kPa and 750 kPa. The difference between measured and computed values is expected due to the uncertainty in exact sensor positions. Nonetheless, both field test outcomes and numerical results align with the pile's response to increased temperature. Similar to the daily temperature changes along the pile, the rate of thermally induced stress increase along the pile length was not constant. The greatest daily stress increase occurred at the end of the first day of heating (day 1), reflecting the temperature change pattern.

This study revealed substantial variability in the cross-sectional distribution of thermally induced stresses along different depths of the pile, corroborating the findings of Abdelaziz and Ozudogru (2016). To illustrate this, Figure 5.8 presents the thermally induced axial stresses in the pile cross-section at four different depths on the third day of the test. Given the variability of stress in the cross-section, this could account for the differences in the measured values of the sensors and pipes, even with minimal deviations from their original positions.

As cooling began, the temperature along the pile decreased, as depicted in Figure 5.4. By the end of the first cooling day (day 4), the highest temperature drops of about 3.0°C was

observed at the top of the pile, due to the significant temperature gradient between the pile and the pipe. The corresponding temperature drop ranged from 3.0°C to 3.6°C for sensors located 11.7 cm and 12.9 cm from the pile center. The rate of temperature decrease was not uniform during the cooling phase, with a greater decline observed as cooling progressed. For example, on days 5 and 6, the measured and computed temperature decreases for the top third quarter of the pile were 4.5~4.9°C and 4.5~5.9°C, respectively. The smallest temperature decrease was recorded at the bottom of the pile. Throughout the cooling period, the lowest pipe inlet temperature reached 8°C, as shown in Figure 3.5. By the end of the cooling phase (day 7), temperature values across the pile converged to nearly the same level, with average measured temperatures of approximately 16.7°C and computed temperatures of 16.8°C. These temperatures were lower than the initial ground temperature before the test, indicating that the cooling operation mitigated the effects of surface solar radiation and wind.

As the cooling process continued, axial compressive stresses in the pile decreased, while axial tensile stresses began to develop, peaking at the end of the cooling period (day 7). By the conclusion of the first cooling day (day 4), axial compressive stresses in the pile's mid-section had almost halved. The most significant reductions in axial stress, in percentage terms, were observed at the top and bottom sections of the pile, respectively. By day 6, the entire pile was under tension, with tensile stresses increasing further as cooling proceeded. The highest tensile stress recorded was -1000 kPa at a depth of around 8.7 meters, near the pile's mid-section. This finding aligns with computed stresses based on assumed sensor positions. In both cooling and heating phases, the highest values for both tension and compression consistently appeared near the pile's mid-section, attributable to the pile's unrestrained behavior under the imposed fixity state. However, discrepancies were noted between measured and computed axial stress values, potentially due to (i) unknown exact sensor locations, (ii) the numerical model's assumption of rigid contact between the pile and soil, and (iii) the transition from heated to cooled states, particularly at the end of day 3. Despite these differences, the field test results, and numerical model outputs showed good agreement in terms of thermally induced axial stresses and temperature distribution along the pile, considering both heating and cooling episodes along with the effects of surface solar radiation and wind.

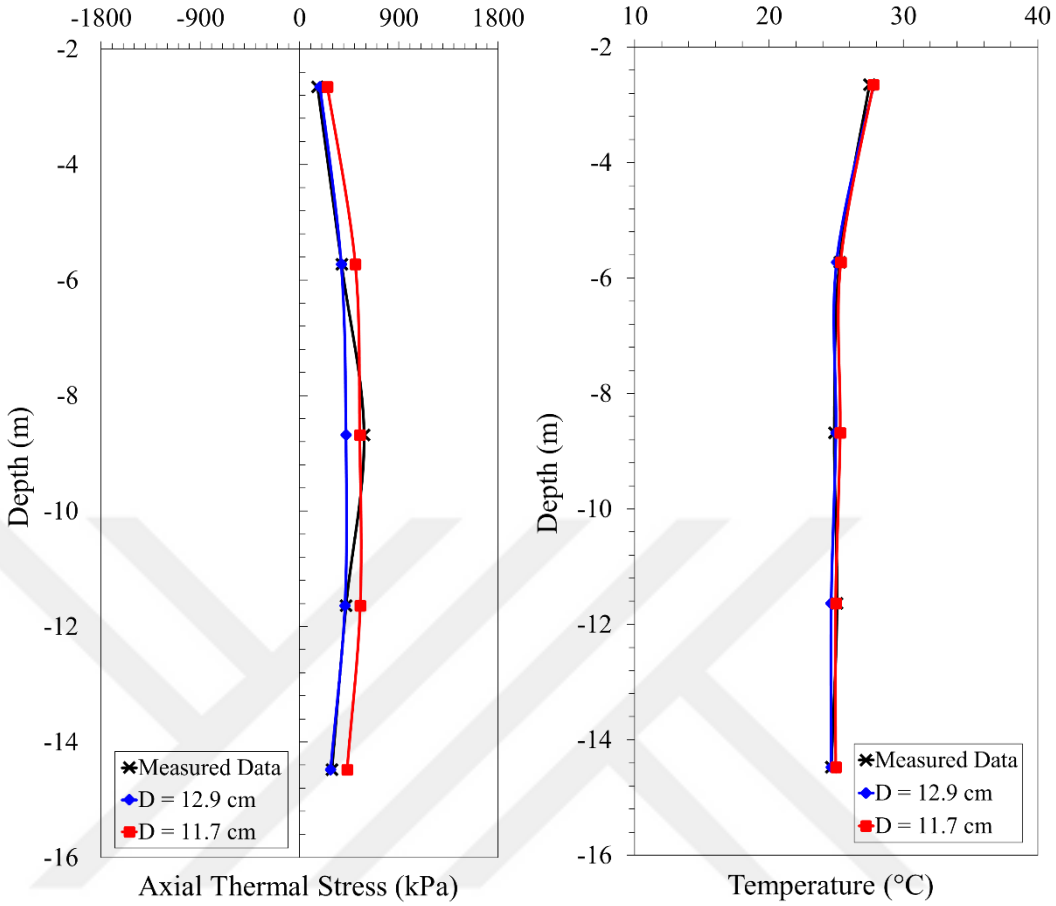


Figure 5.1. Comparison of temperatures and stresses along the pile between the field test and numerical analysis for day-1.

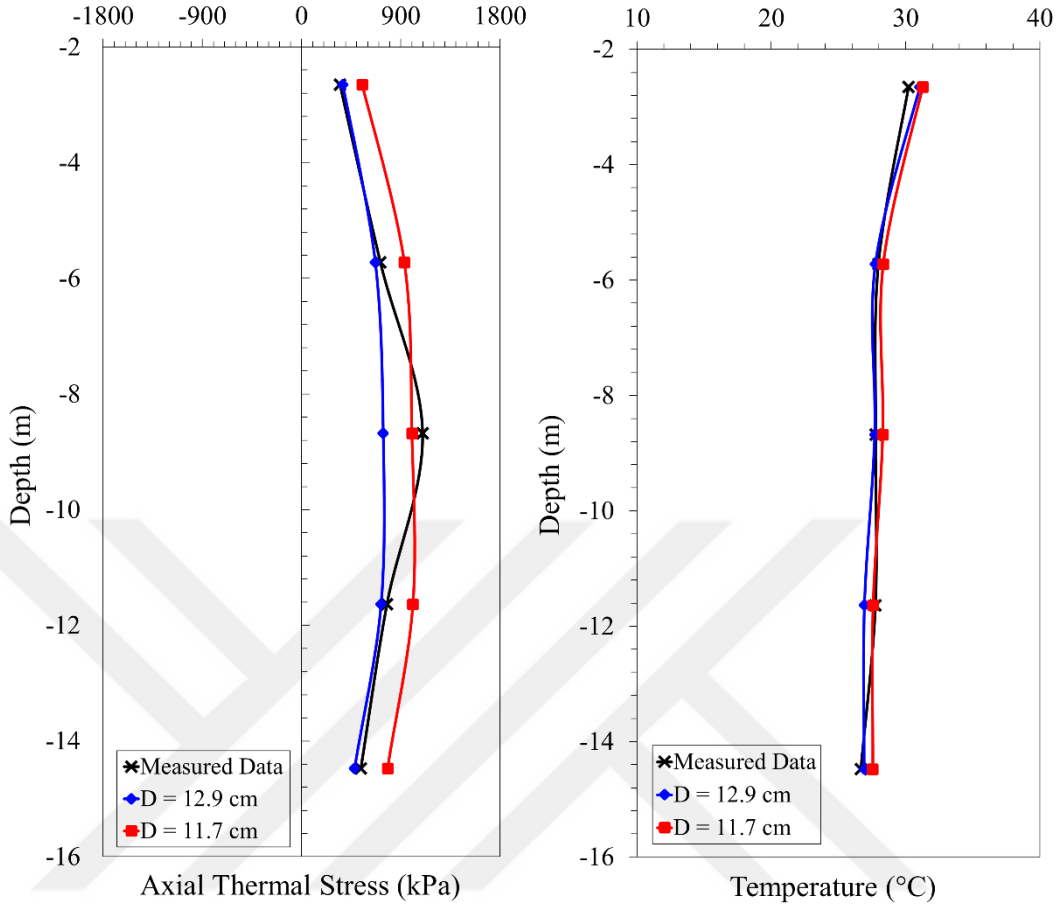


Figure 5.2. Comparison of temperatures and stresses along the pile between the field test and numerical analysis for day-2.

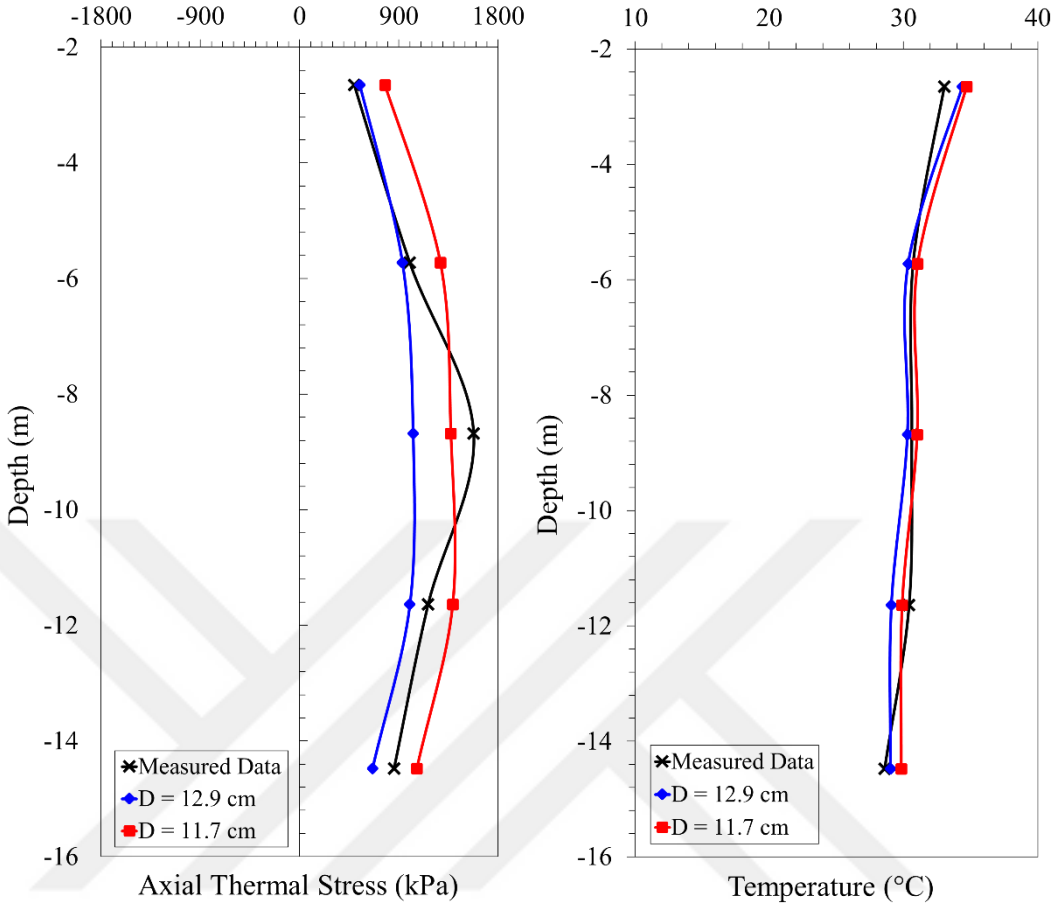


Figure 5.3. Comparison of temperatures and stresses along the pile between the field test and numerical analysis for day-3.

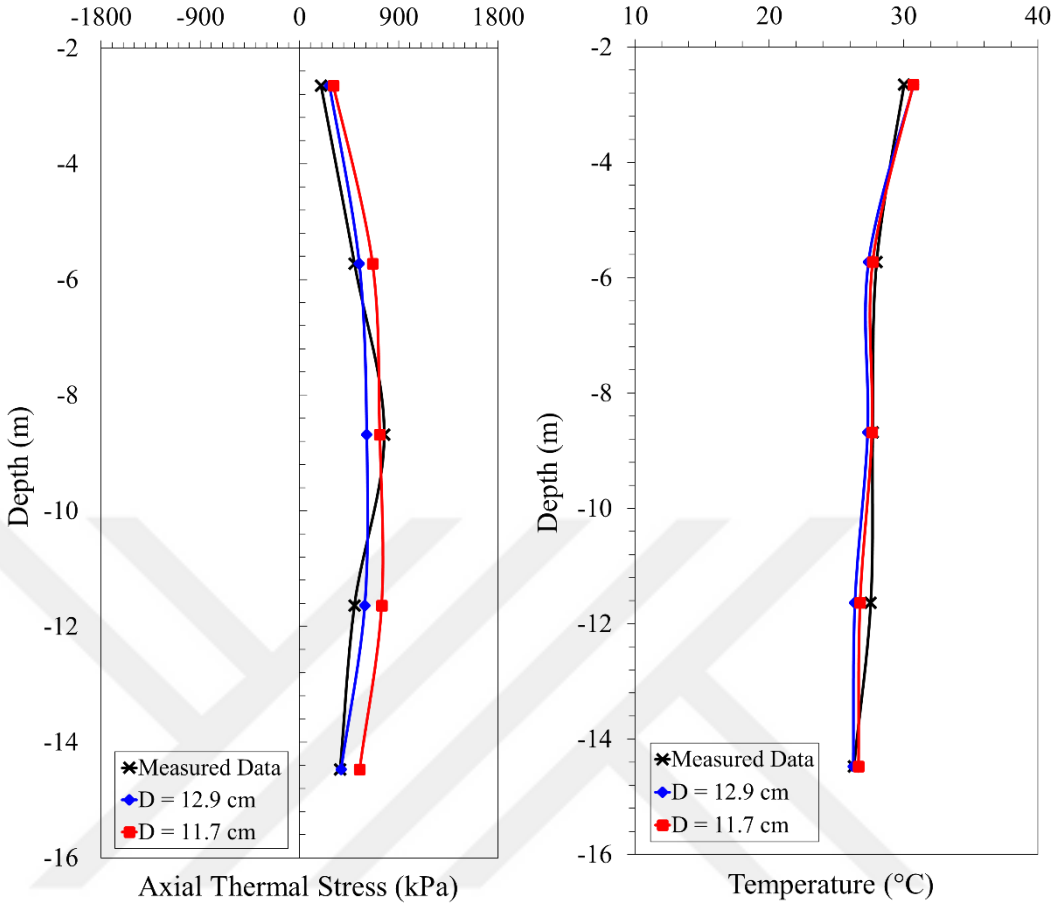


Figure 5.4. Comparison of temperatures and stresses along the pile between the field test and numerical analysis for day-4.

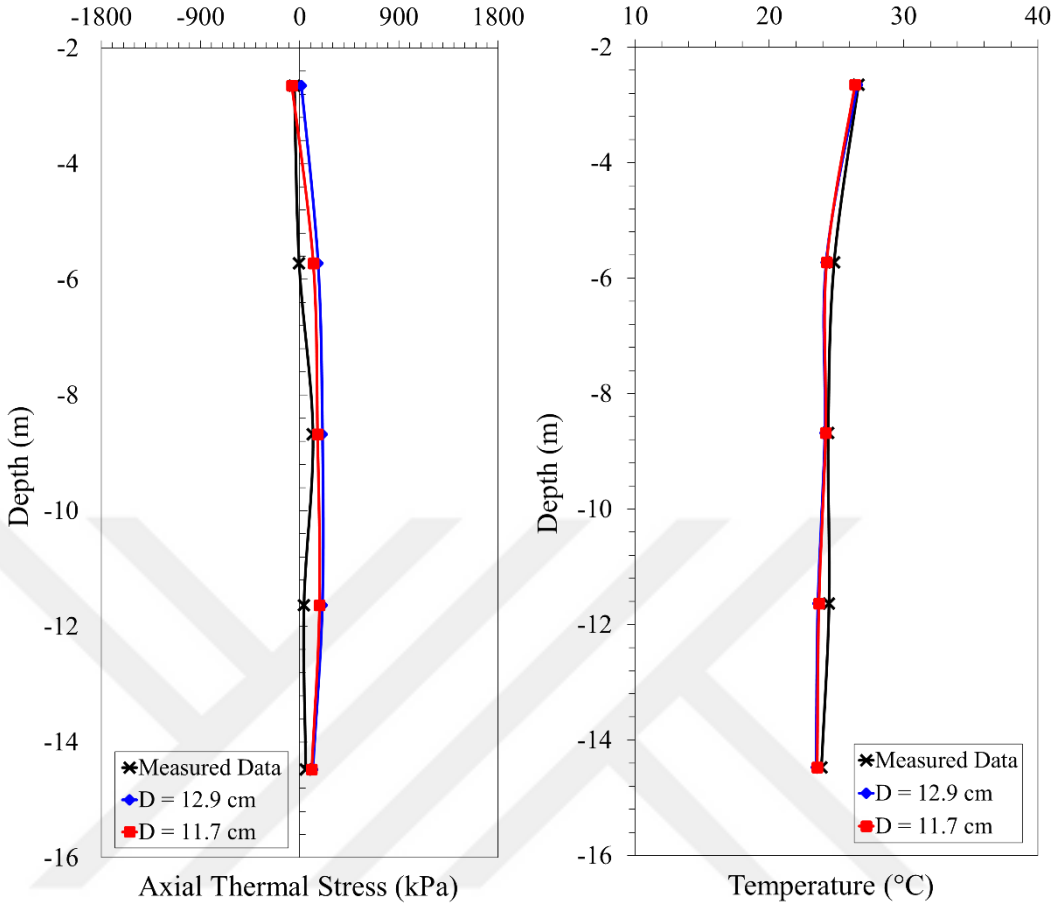


Figure 5.5. Comparison of temperatures and stresses along the pile between the field test and numerical analysis for day-5.

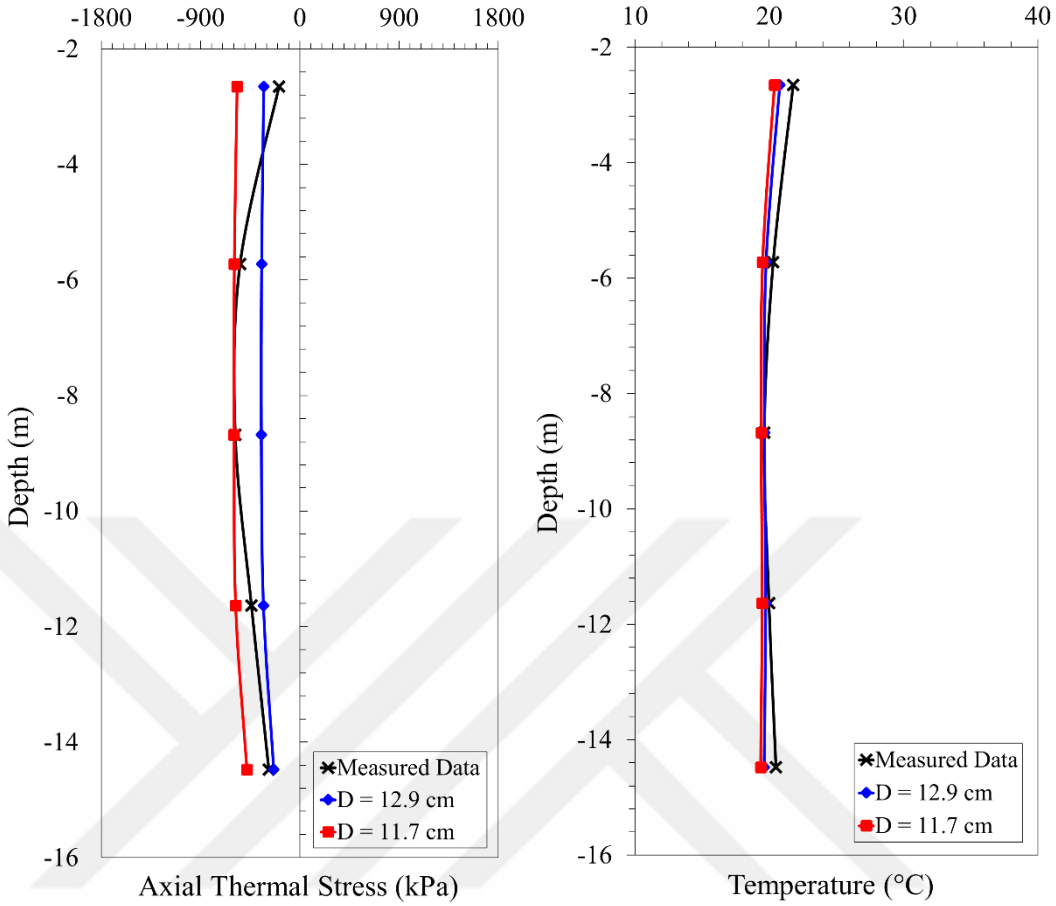


Figure 5.6. Comparison of temperatures and stresses along the pile between the field test and numerical analysis for day-6.

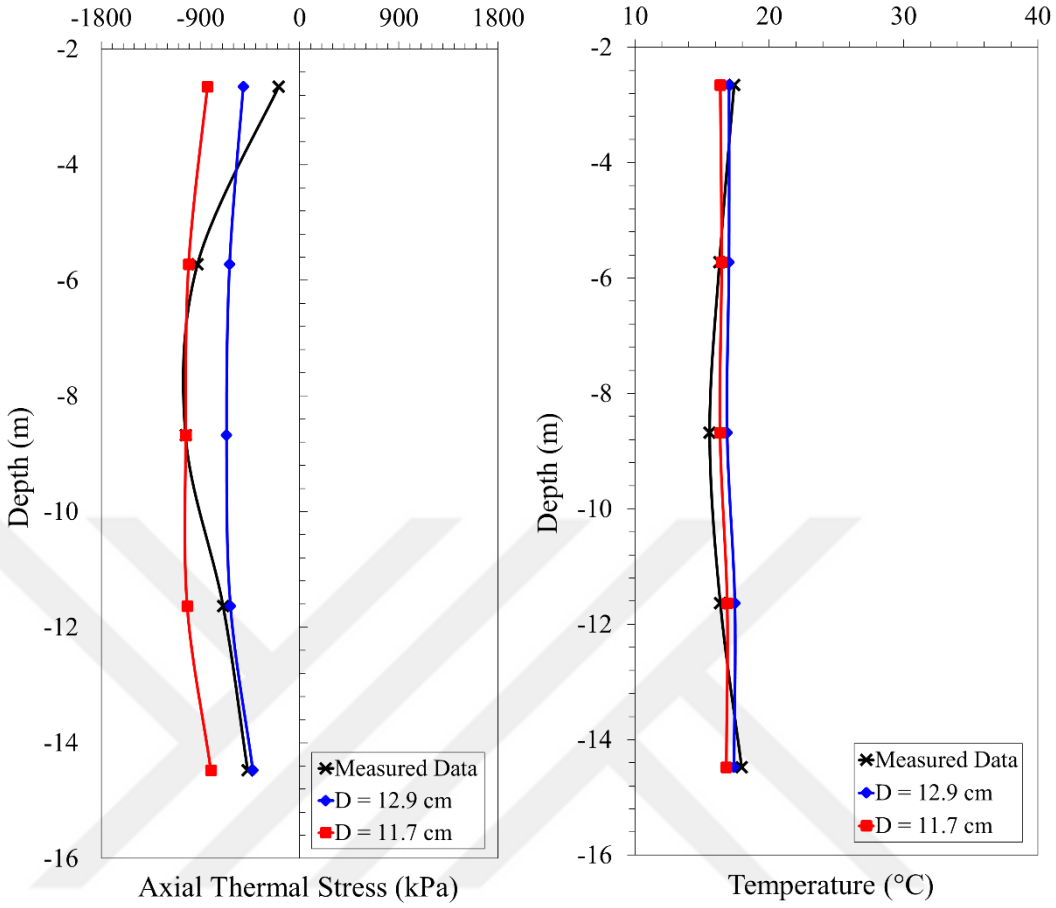


Figure 5.7. Comparison of temperatures and stresses along the pile between the field test and numerical analysis for day-7.

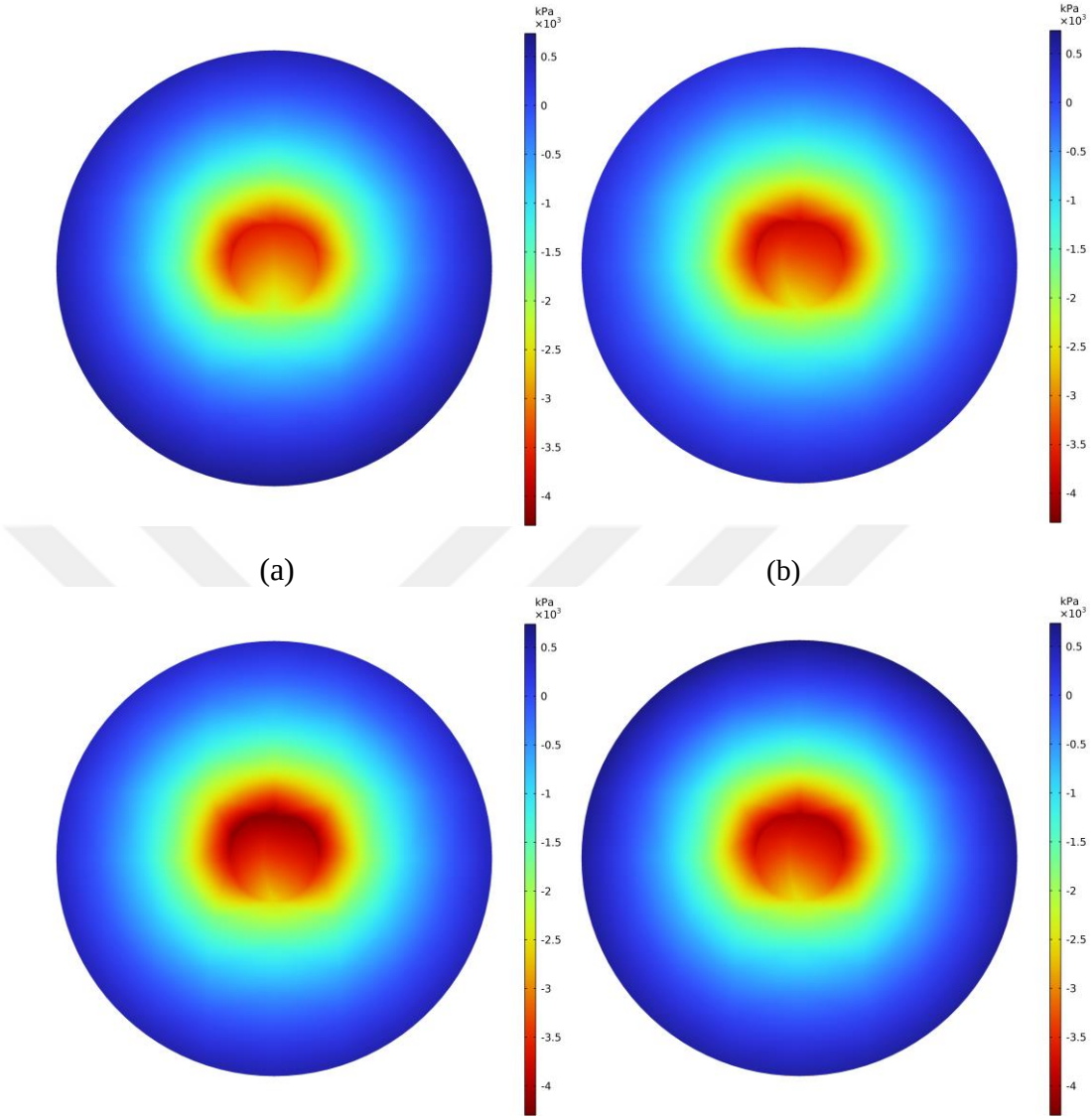


Figure 5.8. Thermally induced axial stresses in pile cross-section on day-3 at (a) 5.7m depth (b) 8.7m depth (c)11.6 m depth (d) 14.5m depth.

6. DISCUSSIONS

6.1. Different Contributions of Solar Radiation and Wind

Understanding the interplay between surface radiation and wind effects is crucial for accurately modelling and predicting temperature variations in various environments. Solar radiation and wind movement typically exert opposite influences on surface temperatures, and therefore, they should be investigated together rather than separately. Solar radiation, with its consistent influx of energy during daylight, tends to increase surface temperatures significantly. This heating effect can be profound, especially in regions with high solar exposure. On the other hand, wind convection acts as a cooling mechanism, transporting heat away from the surface and redistributing it within the atmosphere. This natural cooling effect of wind can moderate the intense heating caused by solar radiation, leading to a more balanced thermal profile at the surface. Analyzing these processes in isolation, however, can lead to unrealistic temperature profiles that do not reflect actual conditions.

To elucidate the combined impact of solar radiation and wind convection, two distinct analyses were undertaken: one focusing solely on solar radiation and the other exclusively on wind effects. Temperature measurements along the pile, derived from simulations considering only solar radiation, only wind, and their combined effects, were compared with initial field temperatures measured prior to pile activation, as depicted in Figure 6.1. These analyses provided a deeper understanding of how each factor individually affects the temperature distribution along the energy pile and highlighted the necessity of integrating both effects for a more accurate and realistic thermal model.

Figure 6.1 highlights that when only solar radiation is considered, at a depth of 2.7 m in the pile, temperatures can soar to 60°C, a scenario far removed from real-world conditions. This extreme temperature spike underscores the significant impact of solar radiation on surface heating. Conversely, in simulations where only wind convection is accounted for, the initial temperature registers lower than the ambient environment due to the lack of solar heating. The resultant heat flux from wind convection, driven by the temperature gradient between the ground surface and the surrounding air, increases ground temperatures under

these conditions. While this approach yields results somewhat closer to reality compared to solar radiation-only simulations, it is not universally applicable. Different climatic conditions, such as those in the Baltic region versus the Arabian Peninsula, could produce varying outcomes, underscoring the need for an integrated analysis of both solar and wind effects to achieve accurate temperature modeling across diverse scenarios.

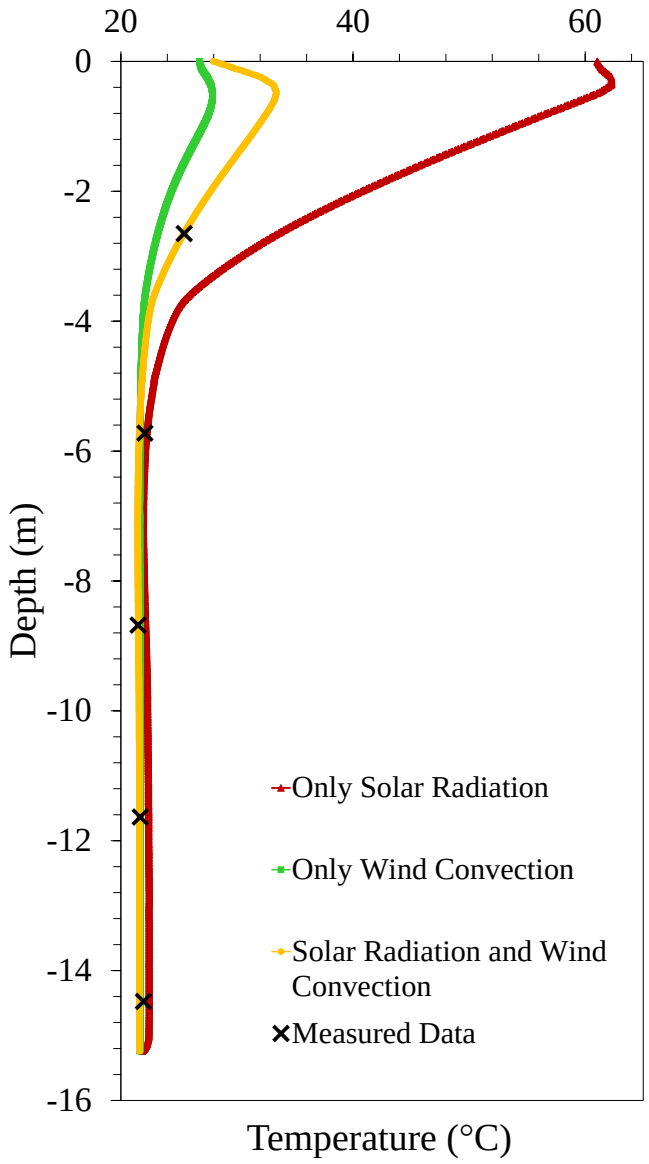


Figure 6.1. Comparison of temperature profiles along the pile obtained in the field and with analyses with solar radiation only, wind convection only and combined effects.

6.2. Applicability of This Modelling Approach

This modelling approach was evaluated within the framework of energy piles in this study. However, the effects noted would not typically be anticipated for energy piles that are directly integrated with a superstructure such as building. The absence of direct connection between the test energy pile and a superstructure allowed for the observation of these effects. Similar effects are expected in various energy geostructures exposed to the ambient environment. Examples include shoring piles, diaphragm walls, horizontal geothermal applications, and piles situated under bridges.

As an example, Wu et al. (2020) examined a row of piles in a bridge, designating one of the piles as an energy pile. They included the temperature variation along the depth in the energy pile before and after thermal activation, and both energy and traditional piles are influenced by atmospheric effects from the surface to a depth of approximately 6 meters, persisting even after thermal activation of the energy pile. This example underscores the broad applicability of the improved modeling approach and its relevance to various types of energy geostructures exposed to environmental conditions.

In scenarios like this, accurate modelling of atmospheric effects is crucial for correctly calculating the efficiencies of both energy and traditional piles, as well as accurately estimating the internal stresses they experience. Additionally, when energy piles are used for de-icing beneath a bridge abutment, heat is extracted from the ground in very cold conditions, leading to the cooling of the surrounding soil. The already cooled soil becomes increasingly vulnerable to freezing during abrupt seasonal temperature fluctuations near the surface. This scenario poses a substantial challenge not only for the operational efficiency of the energy system but also for the structural integrity of the bridge foundation. The expansion of frozen soil can induce heaving and additional stresses on the foundation elements, leading to cracks and other forms of structural damage. Consequently, this can necessitate costly repairs and potentially compromise the overall safety and stability of the bridge structure.

7. CONCLUSIONS

This study provides a comprehensive enhancement to the modeling of energy piles by integrating atmospheric and solar effects into numerical analyses. Traditionally, energy pile models have often overlooked these environmental factors, focusing primarily on adiabatic thermal boundary conditions. However, such an approach overlooks a realistic thermal profile which is essential for designing energy piles that are both accurate and cost-effective. The interaction with atmospheric conditions is crucial in various engineering applications, such as designing energy diaphragm walls, bridge footing piles, horizontal geothermal systems, shoring piles, and embankment dams. This study bridges this gap by incorporating surface solar radiation and wind convection into the numerical model, resulting in more accurate simulations of the thermal responses of both soil and energy piles.

The field test conducted on a continuous flight auger pile in Houston, Texas, served as the foundation for validation. By considering the real-world conditions, including solar radiation and wind effects, the study achieved temperature profiles and thermally induced stresses that closely aligned with field measurements. To achieve this, subsurface boundaries were modelled as adiabatic, except for the top boundary. At this boundary, atmospheric variations and wind effects were included to mimic actual field conditions, ensuring an accurate representation of heat flux convection. The top boundary was also numerically exposed to solar radiation to reflect field conditions. Data on wind and solar radiation were obtained from relevant databases for the field test dates. The model's top boundary was exposed to these conditions for two months before the heating-cooling cycle to match the field temperature profile, which varied up to a depth of 6 meters and remained constant beyond that. This approach effectively simulated the impact of atmospheric temperature changes on ground temperature, drawing on existing research for its methodology (Brandl, 2006; Kalogirou and Florides, 2005). This alignment underscores the improved accuracy and relevance of the model, demonstrating that incorporating atmospheric effects leads to a more realistic representation of temperature changes and their impact on thermally induced stresses within the pile.

Thermal loading, whether from heating or cooling, resulted in uneven temperature changes along the pile. The most significant temperature variations occurred at the top and mid-sections of the pile, with the rate of change decreasing during heating and increasing during cooling. In a CFA energy pile with a free top boundary, axial stresses are directly influenced by the temperature profile. Therefore, numerically computed axial stresses were compared with actual measurements. As expected, the most significant temperature and axial stress changes occurred at the end of the initial days of heating or cooling. Key sections of the pile, identified by stress magnitudes, were the mid-section and upper section, due to the unrestrained response of the pile. Similar to the temperature changes along the pile, the development of thermally induced axial stresses was non-uniform, resulting in both compressive stresses during heating and tensile stresses during cooling. Although the magnitude of thermally induced tension may not be detrimental considering the structural capacity of concrete, it is an important factor in energy pile design.

Furthermore, the study's findings have broader implications beyond the specific case study. The enhanced modeling approach can be applied to various energy geostructures exposed to ambient environmental conditions, such as shoring piles, diaphragm walls, and horizontal geothermal applications. For instance, in bridge foundations where energy piles are used for de-icing, accurate prediction of temperature profiles is crucial to prevent surface freezing and ensure structural integrity. By accurately simulating the thermal responses of these structures, engineers can better design and implement geothermal systems that are both efficient and reliable.

Ultimately, the integration of atmospheric and solar effects into numerical models of energy piles represents a significant step forward in the field of geothermal energy systems. This study provides a robust framework for accurate simulations, enhancing the understanding of the thermal behavior of energy piles and supporting the development of more efficient and reliable geothermal technologies. The research highlights the importance of considering environmental factors in the design and analysis of energy geostructures, paving the way for smarter, more resilient, and energy-efficient built environments. As the world continues to seek sustainable energy solutions, the advancements presented in this

study will be instrumental in promoting the broader adoption of geothermal technologies and ensuring their success in various applications.

REFERENCES

Abdelaziz, S., and T. Y. Ozudogru, 2016, "Non-Uniform Thermal Strains and Stresses in Energy Piles", *Environmental Geotechnics*, Vol. 3, No. 4, pp. 237–252.

Acharjya, K., N. K. Jain, A. Prabhu, B. Saraswat, 2024, "Exploring Geothermal Energy's Potential in Smart Cities Building Climate Control", *E3S Web of Conferences*, Vol. 540.

Adinolfi, M., A. F. Rotta Loria, L. Laloui, and S. Aversa, 2021, "Experimental and Numerical Investigation of the Thermo-Mechanical Behaviour of an Energy Sheet Pile Wall", *Geomechanics for Energy and the Environment*, Vol. 25.

Akrouch G. A., M. Sanchez, and J. L. Briaud, 2020, "Thermal Performance and Economic Study of an Energy Piles System Under Cooling Dominated Conditions", *Renewable Energy*, Vol. 147, No. 2, pp. 2736–2747.

Arzanfudi, M. M., R. Al-Khoury, L. J. Sluys, and G. M. A. Schreppers, 2020, "A Thermo-Hydro-Mechanical Model for Energy Piles Under Cyclic Thermal Loading", Computers and Geotechnics, Vol. 125.

ASHRAE Data Viewer 5.0 [Computer software], 2013, American Society of Heating, Refrigerating and Air-Conditioning Engineers, Georgia, United States.

Aydin, M., A. Sisman, S. Dincer, C. Erdogan, and A. Gultekin, 2013, "Thermal Response Testing and Analytical Prediction of Well Performance in Ground Source Heat Pumps", *11th National Installation Engineering Congress* (In Turkish), Izmir, Türkiye.

Banks, D., 2012, *An Introduction to Thermogeology: Ground Source Heating and Cooling*, [2nd edition], John Wiley & Sons, Chichester.

Batini, N., A. F. Rotta Loria, P. Conti, D. Testi, W. Grassi, and L. Laloui, 2015, "Energy and Geotechnical Behaviour of Energy Piles for Different Design Solutions", *Applied Thermal Engineering*, Vol. 86, pp. 199–213.

Bayer, P., G. Attard, P. Blum, and K. Menberg, 2019, "The Geothermal Potential of Cities", *Renewable and Sustainable Energy Reviews*, Vol. 106, pp. 17–30.

Behbehani, F., and J. S. McCartney, 2022, "Energy Pile Groups for Thermal Energy Storage in Unsaturated Soils", *Applied Thermal Engineering*, Vol. 215.

Bergman, T., F. Incropera, A. Lavine, and D. DeWitt, 2011, *Fundamentals of Heat and Mass Transfer*, Wiley, Hoboken, NJ.

Bourne-Webb, P. J., B. Amatya, K. Soga, T. Amis, C. Davidson, and P. Payne, 2009, "Energy Pile Test at Lambeth College, London: Geotechnical and Thermodynamic Aspects of Pile Response to Heat Cycles", *Geotechnique*, Vol. 59, No. 3, pp. 237–248.

Bourne-Webb, P. J., B. Amatya, and K. Soga, 2012, "A Framework for Understanding Energy Pile Behaviour", *Proceedings of the Institution of Civil Engineers - Geotechnical Engineering*, Vol. 166, No. 2, pp. 170–177.

Brandl, H., 2006, "Energy Foundations and Other Thermo-Active Ground Structures", *Geotechnique*, Vol. 56, No. 2, pp. 81–122.

Brettmann, T., and T. Amis, 2011, "Thermal Conductivity Evaluation of a Pile Group Using Geothermal Energy Piles", *Geo-Frontiers 2011*, Dallas, Texas, United States.

Caulk, R., E. Ghazanfari, and J. S. McCartney, 2016, "Parameterization of a Calibrated Geothermal Energy Pile Model", *Geomechanics for Energy and the Environment*, Vol. 5, pp. 1–15.

Cui, Y., and J. Zhu, 2017, "3D Transient Heat Transfer Numerical Analysis of Multiple Energy Piles", *Energy and Buildings*, Vol. 134, pp. 129–142.

Dai, L., S. Li, L. DuanMu, X. Li, Y. Shang, and M. Dong, 2015, "Experimental Performance Analysis of a Solar Assisted Ground Source Heat Pump System Under Different Heating Operation Modes", *Applied Thermal Engineering*, Vol. 75, pp. 325–333.

Dehghan, B., B., 2018, "Effectiveness of Using Spiral Ground Heat Exchangers in Ground Source Heat Pump System of a Building for District Heating/Cooling Purposes: Comparison Among Different Configurations", *Applied Thermal Engineering*, Vol. 130, pp. 1489–1506.

Di Bari, F., 2019, *Performance-Based Design of Energy Piles in The Framework of Eurocodes*, M.S. Thesis, Politecnico Di Torino.

Di Donna, A., A. F. Rotta Loria, and L. Laloui, 2016, "Numerical Study of The Response of a Group of Energy Piles Under Different Combinations of Thermo-Mechanical Loads", *Computers and Geotechnics*, Vol. 72, pp. 126–142.

Di Donna, A., F. Loveridge, M. Piemontese, and M. Barla, 2020, "The Role of Ground Conditions on the Heat Exchange Potential of Energy Walls", *Geomechanics for Energy and the Environment*, Vol. 25.

Elzeiny, R., and M. T. Suleiman, 2021, "Pull-Out Response of a Laboratory-Scale Energy Pile Subjected to Cooling Cycles", *Journal of Geotechnical and Geoenvironmental Engineering*, Vol. 147, No. 7.

Faizal, M., A. Bouazza, C. Haberfield, and J. S. McCartney, 2018, "Axial and Radial Thermal Responses of a Field-Scale Energy Pile Under Monotonic and Cyclic Temperature Changes", *Journal of Geotechnical and Geoenvironmental Engineering*, Vol. 144, No. 10.

Faizal, M., A. Bouazza, J. S. McCartney, and C. Haberfield, 2019, "Effects of Cyclic Temperature Variations on Thermal Response of An Energy Pile Under a Residential Building", *Journal of Geotechnical and Geoenvironmental Engineering*, Vol. 145, No. 10.

Faizal, M., A. Moradshahi, A. Bouazza, and J. S. McCartney, 2022, "Soil Thermal Response to Temperature Cycles and End Boundary Conditions of Energy Piles", *Journal of Geotechnical and Geoenvironmental Engineering*, Vol. 148, No. 5.

Fang, J., G. Kong, Y. Meng, L. Wang, and Q. Yang, 2020, "Thermomechanical Behavior of Energy Piles and Interactions within Energy Pile–Raft Foundations", *Journal of Geotechnical and Geoenvironmental Engineering*, Vol.146, No. 9.

Fang, J., G. Kong, and Q. Yang, 2022, "Group Performance of Energy Piles Under Cyclic and Variable Thermal Loading", *Journal of Geotechnical and Geoenvironmental Engineering*, Vol. 148, No. 8.

Garakani, A. A., B. Heidari, S. M. Jozani, and O. Ghasemi-Fare, 2021, "Numerical and Analytical Study on Axial Ultimate Bearing Capacity of Fixed-Head Energy Piles in Different Soils", *International Journal of Geomechanics*, Vol. 22, No. 1.

Heidari, B., A. Akbari Garakani, S. Mokhtari Jozani, and P. H. Tari, 2022, "Energy Piles Under Lateral Loading: Analytical and Numerical Investigations", *Renewable Energy*, Vol. 182, pp. 172–191.

He, J., M. Yin, X. Wei, and Z. Wu, 2023, "Optimization of Pipe Circuits in Energy Tunnels", *Underground Space*, Vol. 13, pp. 166-182.

Huang, X., Y. Wu, H. Peng, Y. Hao, and C. Lu, 2018, "Thermomechanical Behavior of Energy Pile Embedded in Sandy Soil", *Mathematical Problems in Engineering*, Vol. 2018.

Kalogirou, S., and G. Florides, 2005, “Measurements of Ground Temperature at Various Depths”, *8th REHVA World Congress*, Lausanne, Switzerland.

Knellwolf, C., H. Peron, and L. Laloui, 2011, “Geotechnical Analysis of Heat Exchanger Piles”, *Journal of Geotechnical and Geoenvironmental Engineering*, Vol. 137, No. 10, pp. 890–902.

Kong, G., J. Fang, X. Huang, H. Liu, and H. Abuel-Naga, 2021, “Thermal Induced Horizontal Earth Pressure Changes of Pipe Energy Piles Under Multiple Heating Cycles”, *Geomechanics for Energy and the Environment*, Vol. 26.

Kong, G., D. Wu, and Y.Q. Wei, 2023, “Experimental and Numerical Investigations on the Energy and Structural Performance of a Full-Scale Energy Utility Tunnel”, *Tunnelling and Underground Space Technology*, Vol. 139.

Laloui, L., M. Nuth, and L. Vulliet, 2006, “Experimental and Numerical Investigations of The Behaviour of a Heat Exchanger Pile”, *International Journal of Numerical and Analytical Methods in Geomechanics*, Vol. 30, No. 8, pp. 763–781.

Laloui, L., and A. F. Rotta Loria, 2020, *Analysis and Design of Energy Geostructures*, Academic Press, Cambridge.

Lee, S., J.G. Speight, S.K. Loyalka, 2007, *Handbook of Alternative Fuel Technologies*, CRC Press, Boca Raton.

Li, Q., L. Chen, and L. Qiao, 2017, “Thermal Effect on Structural Interaction Between Energy Pile and Its Host Soil”, *Advances in Materials Science and Engineering*, Vol. 2017, pp. 1-9.

Li, R., G. Kong, Y. Chen, and Q. Yang, 2021, “Thermomechanical Behaviour of an Energy Pile–Raft Foundation Under Intermittent Cooling Operation”, *Geomechanics for Energy and the Environment*, Vol. 28.

Li, R., G. Kong, G. Sun, and Q. Yang, 2022 “Thermomechanical Behaviors of an Energy Pile–Raft Foundation Under Intermittent Operation with Forced Heat Recharge”, *International Journal of Geomechanics*, Vol. 22, No. 10.

Liu, S., Q. Zhang, J. Liu, W. Cui, and X. Yu, 2023, “A Simple Method for Predicting the Response of Single Energy Pile Considering Temperature Variation of Pile–Soil Interface”, *International Journal of Geomechanics*, Vol. 23, No. 2.

Lou, Y., P. Fang, X. Xie, C.S.A. Chong, F. Li, C. Liu, Z. Wang, and D. Zhu, 2021, “Numerical Research on Thermal Response for Geothermal Energy Pile Groups Under Groundwater Flow”, *Geomechanics for Energy and the Environment*, Vol. 28.

Luo, J., Q. Zhang, H. Zhao, S. Gui, W. Xiang, J. Rohn, and K. Soga, 2019, “Thermal and Thermomechanical Performance of Energy Piles with Double U-Loop and Spiral Loop Heat Exchangers”, *Journal of Geotechnical and Geoenvironmental Engineering*, Vol. 145, No. 12.

Makasis, N., and G. A. Narsilio, 2020, “Energy Diaphragm Wall Thermal Design: The Effects of Pipe Configuration and Spacing”, *Renewable Energy*, Vol. 154, pp. 476-487.

Makasis, N., and G. A. Narsilio, 2021, “Investigating the Thermal Performance of Energy Soldier Pile Walls”, *Geomechanics for Energy and the Environment*, Vol.30.

McCartney, J. S., and K. D. Murphy, 2017, “Investigation of Potential Dragdown/Uplift Effects on Energy Piles”, *Geomechanics for Energy and the Environment*, Vol. 10, pp. 21–28.

Mimouni, T., and L. Laloui, 2015, “Behaviour of A Group of Energy Piles”, *Canadian Geotechnical Journal*, Vol. 52, No. 12, pp. 1913–1929.

Mohamad, Z., F. Fardoun, F. Meftah, 2021, "A Review on Energy Piles Design, Evaluation, and Optimization", *Journal of Cleaner Production,* Vol. 292.

Moradshahi, A., M. Faizal, A. Bouazza, and J. S. McCartney, 2021, "Effect of Nearby Piles and Soil Properties on Thermal Behaviour of a Field-Scale Energy Pile", *Canadian Geotechnical Journal,* Vol. 58, No. 9, pp. 1351–1364.

Moradshahi, A., M. Faizal, A. Bouazza, and J. S. McCartney, 2021, "Cross-Sectional Thermo-Mechanical Responses of Energy Piles", *Computers and Geotechnics,* Vol. 138.

Moradshahi, A., M. Faizal, A. Bouazza, and J. S. McCartney, 2022, "Thermomechanical Responses of Thermally Interacting Field-Scale Energy Piles", *International Journal of Geomechanics,* Vol. 22, No.11.

Najma, A., and J. Sharma, 2021, "Incremental Load Transfer Analysis of an Energy Pile Under Arbitrary Mechanical and Thermal Loads", *Geomechanics for Energy and the Environment,* Vol. 28.

Narsilio, G.A., A. Bidarmaghz, and S. Colls, 2014, "Geothermal Energy: Introducing an Emerging Technology", *International Conference on Advances in Civil Engineering for Sustainable Development,* pp. 141-154.

Ng, C. W. W., A. Farivar, S. M. M. H. Gomaa, and F. Jafarzadeh, 2021, "Centrifuge Modeling of Cyclic Nonsymmetrical Thermally Loaded Energy Pile Groups in Clay", *Journal of Geotechnical and Geoenvironmental Engineering,* Vol. 147, No. 12.

Ng, C. W. W., C. Shi, A. Gunawan, L. Laloui, and H. L. Liu, 2015, "Centrifuge Modelling of Heating Effects on Energy Pile Performance in Saturated Sand", *Canadian Geotechnical Journal,* Vol. 52, No. 8, pp. 1045–1057.

Nguyen, V.-T., 2017, *Thermal and Thermo-Mechanical Behavior of Energy Piles*, Ph.D. Thesis, University of Paris-Est.

Park, S., S. Lee, K. Oh, D. Kim, and H. Choi, 2018, "Engineering Chart for Thermal Performance of Cast-In-Place Energy Pile Considering Thermal Resistance", *Applied Thermal Engineering*, Vol. 130, pp. 899–921.

Peng, C., X. Ding, C. Wang, G. Kong, and D. Wu, 2023, "Thermo-Mechanical Characteristics of Laterally Loaded Energy Piles Under Multiple Heating-Cooling Cycles in Mountain Area", *Journal of Energy Storage*, Vol. 63.

Perić, D., T. V. Tran, and M. Miletić, 2017, "Effects of Soil Anisotropy on a Soil Structure Interaction in a Heat Exchanger Pile", *Computers and Geotechnics*, Vol. 86, pp. 193–202.

Yang, S., X. Ren, and J. Zhang, 2011, "Study on embedded length of piles for slope reinforced with one row of piles", *Journal of Rock Mechanics and Geotechnical Engineering*, Vol. 3, No. 2, pp. 167–178.

Rao, K. G., 2004, "Estimation of the Exchange Coefficient of Heat During Low Wind Convective Conditions", *Boundary Layer Meteorology*, Vol. 111, pp. 247–273.

Ravera, E., M. Sutman, and L. Laloui, 2020, "Load Transfer Method for Energy Piles in a Group with Pile–Soil–Slab–Pile Interaction", *Journal of Geotechnical and Geoenvironmental Engineering*, Vol. 146, No. 6.

Rotta Loria, A. F., and L. Laloui, 2017, "Thermally Induced Group Effects Among Energy Piles", *Geotechnique*, Vol. 67, No. 5, pp. 374–393.

Rotta Loria, A. F., and L. Laloui, 2017, "The Equivalent Pier Method for Energy Pile Groups", *Geotechnique*, Vol. 67, No. 8, pp. 691–702.

Rotta Loria, A. F., and L. Laloui, 2018, “Group Action Effects Caused by Various Operating Energy Piles”, *Geotechnique*, Vol. 68, No. 9, pp. 834-841.

Saggu, R., and K. Sarma, 2023, “Pile Group Response to Thermal Cycles and Associated Alterations in Soil Response”, Journal of *Geotechnical and Geoenvironmental Engineering*, Vol. 149, No. 4.

Saggu, R., and T. Chakraborty, 2015, “Thermal Analysis of Energy Piles in Sands”, *Geomechanics and Geoengineering*, Vol. 10, No. 1, pp. 10-29.

Sanchez M., F. Falcao, M. Mack, J. M. Pereira, G. Narsilio, and L. Guimaraes, 2017, “Salient Comments from an Expert Panel on Energy Geotechnics”, *Environmental Geotechnics*, Vol. 4, No. 2, pp. 135–142.

Sani, A. K., and R. M. Singh, I. Cavarretta, and S. Bhattacharya, 2018, “Heat Storage Performance of a Pile Heat Exchanger Installed in Partially Saturated Swelling Clay”, *7th International Conference on Unsaturated Soils*, Hong Kong, pp. 1–6.

Sani, A. K., and R. M. Singh, 2020, “Response of Unsaturated Soils to Heating of Geothermal Energy Pile”, *Renewable Energy*, Vol.147, pp. 2618-2632.

Sani, A. K., R. M. Singh, T. Amis, and I. Cavarretta, 2019, “A Review on The Performance of Geothermal Energy Pile Foundation, Its Design Process and Applications”, *Renewable and Sustainable Energy Reviews*, Vol.106, pp. 54–78.

Shao, D., G. Jiang, C. Zong, Y. Xing, Z. Zheng, and S. Lv, 2021, “Global Sensitivity Analysis of Behavior of Energy Pile Under Thermo-Mechanical Loads”, *Soils and Foundations*, Vol. 61, No. 2, pp. 283–302.

Soga, K., and Y. Rui, 2016, *Energy geostructures, In S. J. Rees, Advances in Ground-Source Heat Pump Systems,* Woodhead Publishing, Cambridge, pp.185-221.

Stewart, M. A., and J. S. McCartney, 2014, "Centrifuge Modeling of Soil-Structure Interaction in Energy Foundations", *Journal of Geotechnical and Geoenvironmental Engineering*, Vol. 140, No. 4.

Sutman, M., 2016, *Thermo-Mechanical Behavior of Energy Piles: Full-Scale Field Testing and Numerical Modeling*, Ph.D. Thesis, Virginia Polytechnic Institute and State University.

Sutman, M., T. Brettmann, and C. G. Olgun, 2019, "Full-Scale In-situ Tests on Energy Piles: Head and Base-Restraining Effects on the Structural Behaviour of Three Energy Piles", *Geomechanics for Energy and the Environment*, Vol. 18, pp. 56–68.

Sutman, M., C. G. Olgun, and L. Laloui, 2019, "Cyclic load–transfer approach for the analysis of energy piles", *Journal of Geotechnical and Geoenvironmental Engineering*, Vol. 145, No. 1.

Vitali, D., A. K. Leung, S. Feng, J. A. Knappett, and L. Ma, 2022, "Centrifuge Modelling of the Use of Discretely Spaced Energy Pile Row to Reinforce Unsaturated Silt", *Geotechnique*, Vol. 72, No. 7, pp. 618–631.

Wang, B., A. Bouazza, R. M. Singh, C. Haberfield, D. Barry-Macaulay, and S. Baycan, 2015, "Posttemperature Effects on Shaft Capacity of a Full-Scale Geothermal Energy Pile", *Journal of Geotechnical and Geoenvironmental Engineering*, Vol. 141, No. 4.

Wang, C., H. Liu, G. Kong, and C. W. W. Ng, 2017, "Different Types of Energy Piles with Heating–Cooling Cycles", *Proceedings of the Institution of Civil Engineers - Geotechnical Engineering*, Vol.170, No. 3, pp. 220–231.

Wood, C. J., H. Liu, and S. B. Riffat, 2010, "An Investigation of The Heat Pump Performance and Ground Temperature of a Piled Foundation Heat Exchanger System for a Residential Building", *Energy*, Vol. 35, No. 12, pp. 4932–4940.

Wu, D., H. Liu, G. Kong, and C. W. W. Ng, 2020, "Interactions of an Energy Pile with Several Traditional Piles in a Row", *Journal of Geotechnical and Geoenvironmental Engineering*, Vol. 146, No. 4.

Wu, D., G. Kong, H. Liu, Q. Jiang, Q. Yang, and L. Kong, 2021, "Performance of a Full-Scale Energy Pile for Underground Solar Energy Storage", *Case Studies in Thermal Engineering*, Vol. 27.

Wu, D., R. Chen, G. Kong, Y. Miao, G. Niu, and W. Huang, 2024, "A Method for Assessing Non-Uniformity of Thermally Induced Stresses in the Cross-Section of Energy Piles", *Journal of Building Engineering*, Vol. 86.

Xie, J., and Y. Q, 2021, "Heat Transfer and Bearing Characteristics of Energy Piles: Review", *Energies*, Vol. 14.

Yazdani, S., S. Helwany, and G. Olgun, 2019, "Investigation of Thermal Loading Effects on Shaft Resistance of Energy Pile Using Laboratory-Scale Model", *Journal of Geotechnical and Geoenvironmental Engineering*, Vol. 145, No. 9.

Yi, M., Y. Hongxing, and F. Zhaohong, 2008, "Study on Hybrid Ground-Coupled Heat Pump Systems", *Energy and Buildings*, Vol. 40, No. 11, pp. 2028–2036.

Zarrella, A., G. Emmi, R. Zecchin, and M. De Carli, 2017, "An Appropriate Use of the Thermal Response Test for the Design of Energy Foundation Piles with U-Tube Circuits", *Energy and Buildings*, Vol. 134, pp. 259–270.

Zhang, H., and Z. Chen, 2017, "Study on Heat Transfer Performance of Energy Pile in GSHP System", *Procedia Engineering*, Vol. 205, pp. 2393–2400.

Zhao, R., A. K. Leung, and J. A. Knappett, 2022, "Thermally Induced Ratcheting of a Thermo-Active Reinforced Concrete Pile in Sand Under Sustained Lateral Load", *Geotechnique*, Vol. 73, No. 9, pp. 826–839.

Zhou, Y., G. Kong, and J. Li, 2023, “Performance of A Belled Pile Influenced by Pile Head Freedom Response to A Cooling–Heating Cycle”, *Journal of Geotechnical and Geoenvironmental Engineering*, Vol. 149, No. 2.